

Recommended Calibration Procedures for GPM Ground Validation Radars

V. Chandrasekar¹, Luca Baldini², Nitin Bharadwaj³, Paul L. Smith⁴

¹ Colorado State University, Fort Collins, CO

² Institute of Atmospheric Sciences and Climate of National Research Council, Rome, Italy

³ Pacific Northwest National Laboratory, Richland, WA

⁴ South Dakota School of Mines and Technology, Rapid City, SD

Draft n. 10

8 May 2015

Recommended Calibration Procedures For GPM Ground Validation Radars

V. Chandrasekar¹, Luca Baldini², Nitin Bharadwaj³, Paul L. Smith⁴

¹ Colorado State University, Fort Collins, CO

² Institute of Atmospheric Sciences and Climate of National Research Council, Rome, Italy

³ Pacific Northwest National Laboratory, Richland, WA

⁴ South Dakota School of Mines and Technology, Rapid City, SD

Draft

TABLE OF CONTENTS

TABLE OF CONTENTS.....	iii
PREFACE.....	vi
FOREWORD.....	vii
ACKNOWLEDGMENTS.....	x
NOTATION.....	xi
LIST OF FIGURES.....	xiii
LIST OF TABLES.....	xvi
1. INTRODUCTION.....	1
2. CHARACTERIZATION OF RADAR SUBSYSTEMS.....	3
<i>2.1 Transmitter measurements.....</i>	<i>7</i>
2.1.1 Transmitted wavelength (frequency)	7
2.1.2 Transmit pulse: power, duration, shape, spectrum, and repetition frequencies	7
2.1.3 Transmitter measurements summary	9
<i>2.2 Antenna measurements.....</i>	<i>10</i>
2.2.1 Antenna pointing	10
2.2.2 Antenna beam pattern measurements	19
2.2.3 Polarization of the transmitted wave	24
2.2.4 Orientation of the antenna H and V Components	26
2.2.5 Effective Antenna System Gain	27
2.2.6 Antenna gain from sun measurements	28
2.2.7 Channel cross-talk	30
2.2.8 Antenna VSWR and other measurements.	31
<i>2.3 Receiver measurements.....</i>	<i>35</i>
2.3.1 Receiver Calibration	35
2.3.2 Noise Power Levels	37
2.3.3 Receiver Noise Bandwidth and Noise Figure	38
<i>2.4 Dual polarization tests.....</i>	<i>39</i>
2.4.1 Transmit Channels	39
2.4.2 Receive Channels	39
<i>2.5 Waveguide and directional and directional coupler measurements.....</i>	<i>39</i>
2.5.1 Waveguide Losses	39

2.5.2	Directional Couplers	40
3.	END-TO-END CALIBRATION VALIDATION/VERIFICATION METHODOLOGIES	42
3.1	<i>Calibration using point targets</i>	42
3.1.1	Trihedral reflectors	43
3.1.2	Calibration sphere experiments	49
3.2	<i>Use of returns from permanent scatterers</i>	53
3.3	<i>Use of returns from precipitation</i>	54
3.3.1	Differential reflectivity calibration	54
3.3.2	Absolute reflectivity calibration	55
3.3.3	Other polarimetric measurements	57
4.	BUILT IN MONITORING TOOLS AND “AUTOMATIC CALIBRATION”	58
4.1	<i>CSU-CHILL implementation</i>	59
4.2	<i>Implementation for systems with magnetron transmitter</i>	63
5.	CALIBRATION PROTOCOL	66
5.1	<i>Inventory of techniques and equipment</i>	66
5.2	<i>Recommended practice</i>	66
	REFERENCES	70
	Appendix: Tables	72

Draft

PREFACE

Calibration of weather radars has a direct impact on the accuracy of measurements and therefore is critical for most applications. For this reason, calibration has been an active topic of study since the early days of radar meteorology, involving both the research and operational community. More recently the discussion on radar calibration is enriched by new challenges. First, the operational use of dual-polarization radars has created a new set of demands for differential measurements. Secondly, the use of radars in a network has highlighted the importance of best practices and standards to assure that all the radars of the network provide meaningful and comparable measurements. Moreover, modern technology has provided many avenues for automating the calibration process, thereby minimizing errors.

This manual has been developed as for Tier 1 GPM Ground validation Radar, although it aims at a broader audience. It takes a fundamental look at the weather radar calibration process, and illustrates how a collection of consolidated techniques and modern technologies can be used to the purpose of calibrating radar, with special attention to dual polarization systems.

This manual is organized as follows: The introduction aims to introduce the problem of calibration using a high level view of the radar divided into subsystems that are useful for calibration. Subsequently procedures to characterize radar subsystems, particularly transmitter, antenna, and receiver are presented. Many of the described techniques make use of external sources, such as the Sun or installations using standard gain horns to characterize performance of two subsystems (e.g. transmitter-antenna or antenna-receiver). Since a radar is a complex system, characterization of each of its many components is not easy and therefore, calibration of radar subsystems must be complemented with methods allowing an end-to-end calibration of the radar. Methods based on the use of artificial targets (metallic spheres or corner reflectors) or natural sources (meteorological scatterers) are illustrated. An example, implemented on CSU-CHILL radar, of how modern technologies can be used to monitor radar calibration parameters is finally provided.

FOREWORD

Operational and research radar use to estimate quantities such as precipitation rate and type over scales ranging from regional to continental is prolific. Of course, radars do not actually measure precipitation rate or type; rather those quantities are inferred from radar-measured parameters such as returned echo power and phase from a given volume of precipitation. Thus in order to claim we are “measuring” a precipitation rate we must apply a conversion between calibrated returned power and rainfall rate. We are thus able to create a map of rainfall at kilometer or better spatial resolution, over areas of $\sim 10^4$ km² or larger, and on time scales of minutes. Having this capability is powerful, enabling a host of hydrologic applications not the least of which are flood prediction and water resource management. Importantly, the ability to use calibrated radars to map rainfall, precipitation types, and 3-D precipitation structures over large spatial domains also provides an important means to validate similar measurements made from spaceborne platforms, effectively enabling information content provided by local radar measurements to have a global impact by virtue of improving, verifying etc. global satellite-based precipitation retrievals.

Based on ground validation (GV) use of radar for the Tropical Rainfall Measurement Mission (TRMM), it was concluded early in the planning phases of the Global Precipitation Measurement (GPM) Mission that validation of GPM satellite products should continue to rely heavily on the use of ground-based and airborne radars. From a GPM Ground Validation science perspective well-calibrated ground-based radars represent the primary “scale-translator” between points (e.g., individual rain gauges), regional, and global scale (e.g., satellite) estimates of precipitation rate and accumulation. Given a few lessons learned from TRMM GV radar quality control and validation experiences and a priori expectations of accuracy defined for GPM products, we decided to take a somewhat measured approach to using radar for GPM GV, placing a strong emphasis on the “quality” (as opposed to quantity) of the radar data used, to include a clear expectation and articulation of radar calibration and estimation uncertainty.

At the most basic level radar data “quality” and associated uncertainties in rainfall estimation often trace back to the engineering calibration of the radar measurement itself. Accordingly, one can pose the important question of what is meant by “calibrated” when discussing radar measurements. Moreover, during and subsequent to the GPM era if a priori requirements for

GV radar calibration can be defined how might GV radars achieve a status of “well-calibrated” and hence be included as GV platforms? Indeed, even though it can be argued that advances in technology between the TRMM and GPM eras have generally improved radar products and vastly enhanced our abilities to discern precipitation microphysical processes, in many respects the problem of calibration has become more complicated; e.g., consider the TRMM/GPM-era ground radar technology transition to dual polarization and attendant increases in the number of parameters used for production of radar-based precipitation measurements in research, and now several operational radar networks.

With the aforementioned in mind, it became clear to Arthur Hou and I that some form of unified calibration approach, consisting of both a description of methodology and the means to implement the methodology was needed. Under Arthur’s leadership as the GPM Project Scientist we proceeded to discuss this need with the international community at several GPM Ground Validation meetings, and we pursued the issue more explicitly with Professor Chandrasekar (Chandra) and Dr. Baldini (Luca). Luckily for the reader and the radar community alike Chandra and Luca graciously honored our request to translate their extensive radar calibration experience into this publication, a document that details an orderly set of steps to achieve a robust engineering radar calibration.

Herein the notion of an “engineering calibration” characterizing individual radar sub-systems and the means to calibrate each sub-system is described. The document provides a helpful and quick introduction that describes the radar equation in the context of the calibration exercise. The following chapters include calibration protocols providing detailed approaches for calibrating individual transmitter and receiver component sub-systems, but also include simpler methods for system-level calibration. For example, straight forward techniques to calibrate radar returned power using spheres and corner reflectors are provided. Similarly, methods to calibrate system dual-polarization variables using the sun or vertically-pointing in light rain are included. A listing of recommended calibration practices and even the equipment necessary to achieve each step is also provided at the end of the document.

Collectively, Chandra and Luca have produced exactly what Arthur and I were looking for relative to documenting a straight forward approach to radar “calibration”, thus assuring “quality” GV radar data if implemented. From a my perspective the publication really documents/formalizes a set of standard calibration practices that the broader radar community already exercises in many instances and hence could almost certainly “buy into”. More practically, the “Recommended Calibration Procedures for GPM Ground Validation Radars” provides a basis for assuring that we can minimize uncertainty in precipitation estimates due to instrument error. This is important because in our quest to provide top notch precipitation estimates for GPM GV, reducing or accounting for instrument error will enable improved

radar-based estimates of precipitation, more robust verification of GPM satellite estimates of precipitation, and improved interpretation of precipitation microphysics toward improving satellite-based precipitation retrieval algorithms.

Walter A. Petersen, NASA GPM GV Science Manager

Arthur Y. Hou, (1947-2013), NASA GPM Project Scientist

Draft

ACKNOWLEDMENTS

We graciously acknowledge all our collaborators, our teachers and students who educated us in various forms that resulted in the knowledge described in this document. We acknowledge NASA GPM program for providing a platform to prepare this handbook. In addition, we acknowledge the other agencies, specifically DOE and NSF who supported the calibration activities. We acknowledge Drs David Hudak, and Tomoo Ushio who served as early reviewers on the concepts to be covered in this handbook.

NOTATION**List of symbols**

τ	Transmit pulse duration	S
λ	Wavelength	M
σ	Corner reflector radar cross section	m ²
θ_1	Antenna 3-dB azimuth beamwidth	Radians
ϕ_1	Antenna 3-dB elevation beamwidth	Radians
v_d	Mean Doppler velocity	m s ⁻¹
\hat{P}_{cr}	Digitized received power from corner reflector	Dimensionless
$ K_w ^2$	Dielectric factor of water	dimensionless
<i>AZ</i>	Azimuth	degree
<i>B</i>	Bandwidth of a radar receiver	Hz
<i>c</i>	Speed of light	m s ⁻¹
<i>e_a</i>	Antenna aperture efficiency	dimensionless
<i>EL</i>	Elevation	degree
<i>f</i>	Transmit frequency	Hz
<i>G₀</i>	Antenna gain	dimensionless
<i>G_c</i>	Net RF-to-IF conversion gain	dimensionless
<i>G_e</i>	Effective antenna system gain	dimensionless
<i>G_r</i>	Receiver gain	dimensionless
<i>G_t</i>	Gain of a standard horn	dimensionless
<i>K</i>	Boltzman constant (1.38×10^{-23} J K ⁻¹)	
<i>l_d</i>	Two-way radome loss	dimensionless
<i>l_n</i>	Near-field antenna gain loss for point target	dimensionless
<i>l_p</i>	Probert-Jones integral correction	dimensionless
<i>l_r</i>	Receiver finite bandwidth power loss	dimensionless
<i>l_{rp}</i>	Receive path loss	dimensionless
<i>L_p</i>	Transmit path loss	dimensionless
<i>P_{av}</i>	Average transmit power	W
<i>PRF</i>	pulse repetition frequency	Hz
<i>P_t</i>	Transmit peak power	W
<i>R_{cr}</i>	Slant range to corner reflector	m
<i>SFU</i>	Solar flux unit	W Hz ⁻¹ m ⁻²
<i>SNR</i>	Signal to noise ratio	dimensionless
<i>T</i>	Temperature	K
<i>Z_{dr}</i>	differential reflectivity	dimensionless

Z_e, Z	Equivalent reflectivity factor	$\text{mm}^6 \text{m}^{-3}$
Φ_{dp}	differential propagation phase shift	$^{\circ} \text{km}^{-1}$
ρ_{hv}	Copolar correlation coefficient	dimensionless

Abbreviations

AFC	Automatic frequency control
CSU-CHILL	Colorado State University–University of Chicago/Illinois State Water Survey Radar
CW	Continuous wave
D3R	NASA Dual-frequency, Dual polarized, Doppler radar
GQ	Gunner’s quadrant
IF	Intermediate frequency
LNA	Low Noise Amplifier
RSP	Radar Signal Processor
SA	Spectrum Analyzer
SACR	Ka-band Scanning ARM Cloud Radar
SNR	Signal to Noise Ratio
SSU	Solar Scan Utility
STAR	Simultaneous transmit and receive
VSWR	Voltage Standing Wave Ratio

LIST OF FIGURES

Figure 1: Thematic diagram of a weather radar; separate antennas are shown here for transmitting and receiving, but in most radar systems both functions share a common antenna.....	2
Figure 2: Thematic diagram of a weather radar for calibration purposes.	5
Figure 3: A pyramidal standard gain horn antenna at CSU-CHILL facility.....	6
Figure 4: Different shapes of pulses with different durations (Polar 55C radar, CNR, Italy).	9
Figure 5: A gunner’s quadrant measurement on a flat surface being made by one of the authors (PLS) at CSU-CHILL radar facility.	12
Figure 6: Example of gunner’s quadrant (GQ) data checking the leveling of the CSU-CHILL antenna pedestal; the GQ can be read to a precision of 0.005 deg, and the 0.01 deg amplitude of the fitted sinusoid indicates that the pedestal is level to within about 0.01 deg. (The data offset from zero here is of no consequence; the antenna structure need not be at zero elevation during the antenna rotation in azimuth.).....	13
Figure 7: Plot of errors in the indicated elevation angle increment (from an approximately plumb starting orientation) versus the actual increments measured with a gunner’s quadrant. No easy access is available to establish a plumb orientation of the CSU-CHILL antenna, so the reference orientation was an indicated elevation angle of 0.01 deg (One high-elevation data point, lying almost 0.3 deg away from the others, was omitted from the plot as probably due to a reading error.).....	14
Figure 8: Example plot of error in indicated elevation angle increment (from plumb antenna) vs. true angle increment measured with gunner’s quadrant (GQ); points denoted by open triangles represent repeated measurements.	15
Figure 9: Example plot of nonlinear elevation data errors, as determined from solar scans with an SSU.	16
Figure 10: Example plot of solar-scan (absolute) and GQ (relative) elevation-error data overlaid on a common plot. Only the GQ “upward” data are included here because the SSU employed for the solar scans works upward from below the sun.....	17
Figure 11: Example plot of data from clockwise and counter-clockwise traverses, at a fixed elevation angle, across the location of a standard-gain horn in the far	

field radiating a CW signal. The offset between the two curves indicates backlash of 0.09 deg in the azimuth data linkage (CSU-CHILL radar).	20
Figure 12: Color plots of antenna beam patterns obtained with the standard-gain horn radiating a test signal. Top: H-channel antenna beam patterns obtained with the horn radiating (left) an H-polarized and (right) a 45-deg- polarized signal. Bottom: corresponding plot of the V-channel antenna beam pattern obtained with the standard-gain horn radiating a V-polarized signal.	22
Figure 13: Example of data from an azimuth cut through the antenna beam axis. With these semi-log scales, the parameters of a parabola fit to the points near the axis determine the 3 dB beamwidth.	23
Figure 14: Example of received power pattern (horizontal polarization) obtained via a solar scan with the D3R radar at Ku (left), and Ka band (right).	24
Figure 15: Power received at standard-gain horn as a function of the horn rotation angle, for a case where the polarization of the radiated signal is nearly circular (0 deg indicates vertical polarization for the horn).	25
Figure 16: Power received at standard-gain horn as a function of the horn rotation angle, for a case where the polarization of the radiated signal is elliptical. (0 deg indicates vertical polarization for the horn).	26
Figure 17: Example plot of results with obtained with a rotated horn transmitting to the radar.	27
Figure 18: Antenna gain estimated weekly using solar calibration in H and V channels from May to September, 2003 (CSU-CHILL).	30
Figure 19: Example plot of detected envelopes of transmitted pulse and reflected signal in the CHILL H channel; signal magnitudes have been adjusted to facilitate timing comparisons.	32
Figure 20: Example of results from a Network Analyzer sweep of the Return Loss (here given with a negative sign) in the waveguide of an S-band radar operating at about 2806 MHz.	34
Figure 21: Example of receive calibration plot (CSU-CHILL radar).	36
Figure 22: Example of data from a Network Analyzer sweep of the loss in dual-polarized radar.	41
Figure 23: Calibrated 60-dB cross-guide directional coupler at the output of a klystron transmitter (Polar 55C, CNR; Italy). For most calibration purposes in-line bidirectional couplers are more useful.	41
Figure 24: Geometry of a triangular trihedral corner reflector. The line of view is the direction of the bore sight of the antenna beam with respect to the corner reflector.	44
Figure 25 : Illustration of the setup for calibration with a triangular trihedral corner reflector.	44

Figure 26 : Bounds on the bias in received signal power from corner reflector as a function of signal-to-clutter ratio.	47
Figure 27 : Received power (relative to corner reflector) of a 55 feet tower with and without a trihedral corner reflector. The observations were made with Ka-band Scanning ARM Cloud Radar (Ka-SACR).....	47
Figure 28 : The antenna pattern of Ka-SACR from test range along with the simulated far field and Fresnel region antenna pattern.....	48
Figure 29 : Comparison of corner reflector observations without (left) and with (right) precipitation.....	49
Figure 30: Preparation of a free-flying sphere for a calibration experiment at CSU CHILL facility supervised by one of the authors (VC).....	51
Figure 31: Normalized radar cross section of a metallic sphere as a function of the normalized diameter.	52
Figure 32: Estimation of antenna gain using data from a sphere calibration experiment.....	52
Figure 33: Comparisons of the directly-measured transmit pulse and the estimated pulse waveform from the sphere return (<i>CSU-CHILL, experiment of September 23, 2011</i>).....	53
Figure 34: Example of the scatter of vertically-pointing Z_{dr} measurements as a function of azimuth during antenna rotation (Polar 55C measurements).....	56
Figure 35: CSU-CHILL radar configuration. Different colors are used to distinguish radar subsystems. Orange boxes identify calibration subsystem. Only one polarization channel is shown.	60
Figure 36: Configuration of Figure 35 in the normal receive mode.	60
Figure 37: Configuration of Figure 35 for pulse transmission measurements.....	61
Figure 38: Configuration of Figure 35 for LNA and downconverter gain calibration mode.....	61
Figure 39: Configuration of Figure 35 for downconverter gain calibration mode.....	62
Figure 40: Configuration of Figure 35 to determine the receiver's noise figure	63
Figure 41: Configuration of calibration paths of a radar with magnetron transmitter using a calibrated source. Receiver and transmitter calibration paths are shown in dash and dot lines, respectively.	65

LIST OF TABLES

Table 5.1 – Summary of calibration equipment.....	68
Table 5.2 – Summary of calibration practices	69

Table in appendix

Table 1: Summary of Transmitter Power Measurements	73
Table 2: Antenna Gain Measurements (horn transmitting to radar antenna).....	74
Table 3: Antenna Gain Measurements (horn receiving method).....	75
Table 4: Antenna Gain Measurements (solar calibration)	76
Table 5 - Return-Loss Measurements	77
Table 6 - Summary of RSP Calibrations.....	78
Table 7 - Some Characteristics of the FIR Filter	79
Table 8 - Receiver Noise Levels	80
Table 9 - Noise Figure/Bandwidth Measurements	81
Table 10 - Radar average power received at horn (up-link)	82
Table 11 - Test signals received (at IF) in H and V channels (downlink)	83
Table 12 – Waveguide measurements	84
Table 13 - Directional couplers.....	85

Draft

1. INTRODUCTION

The concept of calibration of a weather radar system covers multiple aspects. Fundamentally, a weather radar measures backscattered echo from precipitation and produces derived variables such as equivalent radar reflectivity factor (denoted by the symbol Z_e and expressed in units of $\text{mm}^6 \text{m}^{-3}$), differential reflectivity (Z_{dr}), mean and standard deviation of the Doppler velocity spectrum, differential propagation phase (Φ_{dp}), the copolar correlation coefficient (ρ_{hv}), and some additional variables depending on the type and configuration of radar system. This document will focus primarily on calibration of reflectivity and differential reflectivity measurements, while system check procedures will be discussed for monitoring copolar correlation, Doppler velocity and differential phase.

While the calibration of radar variables such as reflectivity is important, the radar provides information on these quantities as a function of three-dimensional positions in polar coordinates. Therefore, position calibration is also very important in a weather radar system. The positioning in a mechanically scanning radar system is accomplished through azimuth and elevation positioners, and the angle data are typically derived from synchros or shaft-position encoders. The range to a radar echo is determined electronically from timing considerations, and timing measurements in radar are fairly accurate.

In this document an introduction of radar as a system is provided first to define the various aspects of calibration. Subsequently, system check procedures are described from the perspective of “knowing the system behavior or characteristics.” To help understand radar as a system, it can be broadly divided into transmitter, receiver, and antenna subsystems, the propagation medium, and the scatterer(s) (Figure 1). To characterize the scattering object or objects within the illuminated volume, the transmitter, receiver and antenna should be characterized well; in addition, we need to understand the propagation medium behavior. The transmitter determines the characteristics of the radiated signal (frequency, modulation and amount of transmitted power), whereas the pointing of the antenna determines the direction of transmission and the type of antenna determines the signal polarization.

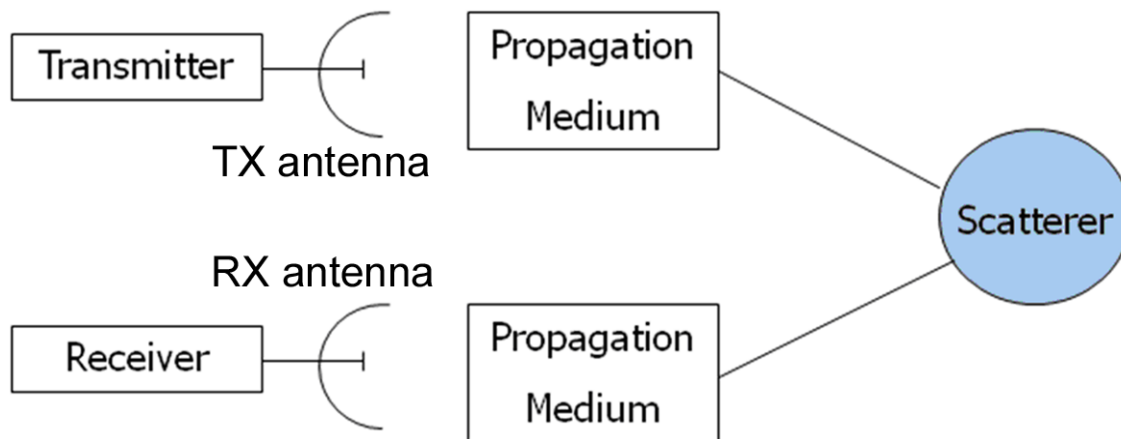


Figure 1: Thematic diagram of a weather radar; separate antennas are shown here for transmitting and receiving, but in most radar systems both functions share a common antenna.

Radar is a complex system consisting of many components such as signal oscillators, receivers, amplifiers, filters, and microwave components. A typical radar system has too many components to make it feasible to characterize every component. For this reason, it is usually more useful to evaluate and characterize the system in terms of its major subsystems.

2. CHARACTERIZATION OF RADAR SUBSYSTEMS

The most important or commonly encountered calibration of weather radar is the calibration of the equivalent reflectivity factor or Z_e . For us to understand calibration to characterize the measurement of Z_e , it is useful to take a look at the weather radar equation. In radar meteorology it is conventional to express volumetric reflectivity η in terms of the equivalent reflectivity factor as

$$Z_e = \frac{\lambda^4}{\pi^5 |K_w|^2} \eta \quad (1)$$

where λ is the radar wavelength and the dielectric factor $|K_w|^2$ is computed for water. The received power at the radar at a chosen reference point (typically at the output port of the antenna, the forward port of a directional coupler or sometimes the input to the first amplifier or LNA), can be expressed as

$$P_r(r) = \left(\frac{c\tau}{2} \right) \left[\frac{P_t G_o^2}{(4\pi)^3} \right] \left(\frac{\pi\theta_1\phi_1}{8\ln 2} \right) \left(\frac{\pi^5 |K_w|^2}{\lambda^2} \right) \frac{Z_e(r)}{r^2} \quad (2)$$

where the various quantities are defined according to a standard weather radar equation (Bringi and Chandrasekar, 2001).

Therefore, when the receiver sees power P_r at a time Δt after the pulse transmission, the range r is obtained as $r = c \Delta t/2$ and the above equation is used to compute reflectivity as

$$Z_e = \left(\frac{2}{c\tau} \right) \left[\frac{(4\pi)^3}{P_t G_o^2} \right] \left(\frac{8\ln 2}{\pi\theta_1\phi_1} \right) \frac{\lambda^2}{\pi^5 |K_w|^2} r^2 P_r \quad (3)$$

Based on this the minimum detectable reflectivity at range r for unity SNR can be expressed as

$$\min(Z_e) = \frac{1}{\pi^5 |K_w|^2} \left(\frac{2}{c\tau} \right) \left[\frac{(4\pi)^3}{P_t G_o^2} \right] \left(\frac{8\ln 2}{\pi\theta_l \phi_l} \right) \lambda^2 r^2 (kTB) \quad (4)$$

The receiver and processor, in a general sense, determine how weak a signal can be measured. The received signals are processed through a filter (usually at IF) to enhance the signal-to-noise ratio and that results in some signal loss. Accounting for that, the IF power received from range r can be written as

$$\bar{P}_r(r_0) = \left(\frac{G_r}{l_r} \right) \left(\frac{c\tau}{2} \right) \left[\frac{P_t G_o^2}{(4\pi)^3} \right] \left(\frac{\pi\theta_l \phi_l}{8\ln 2} \right) \left(\frac{\pi^5 |K_w|^2}{\lambda^2} \right) \frac{Z_e(r)}{r^2} \quad (5)$$

where G_r is the receiver gain and $l_r (>1)$ represents the filter loss.

Figure 2 shows the power measurements at the reference plane, which could be anywhere between the circulator and the antenna but is usually at a directional coupler nearer the circulator. It is important to establish such a common reference plane not only for the measurements of transmitted power but also for measurements of effective antenna system gain (Sec. 2.2.5) and for the receiver calibration (Sec. 2.3).

A radar is composed of three main subsystems, namely transmitter, antenna, and receiver (or receiver and signal processor). Each subsystem can in turn be decomposed into several discrete components. As a consequence, a radar system has so many components that it is difficult to be able to characterize every component. For this reason it is sometimes convenient to evaluate and characterize the radar system as a whole. However, to obtain diagnostic information, it is often useful to consider the main subsystems and characterize each single subsystem individually or to consider combinations of two subsystems, such as the set of transmitter and antenna and the set of antenna and receiver.

For the sake of this characterization, many methods described in this section make use of external, or “known,” sources such as the sun or an external transmitter (with a standard antenna), and a receiver that can allow one to characterize more than one subsystem.

The pyramidal standard gain horn (Figure 3) useful in this work is a composed of four conductive planes to form a pyramid of rectangular base terminated with a flange for

connecting it to a waveguide. The nominal gain is provided by the manufacturers as a function of wavelength and polarization.

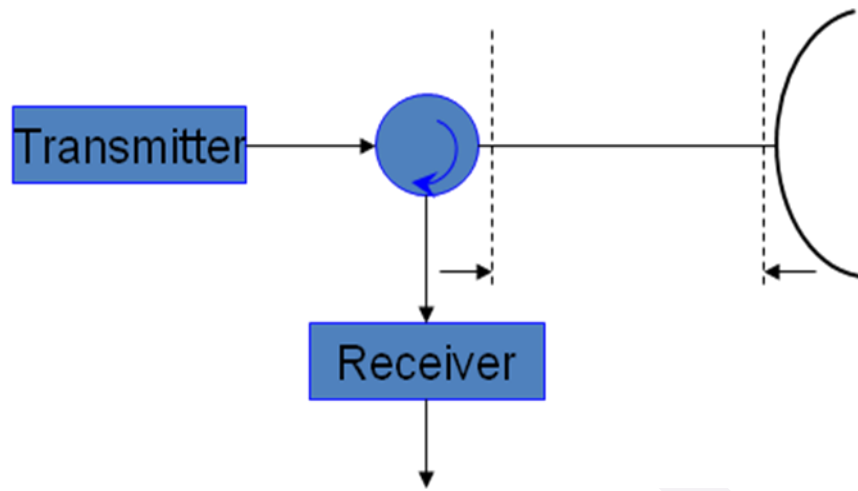


Figure 2: Thematic diagram of a weather radar for calibration purposes.

A standard gain horn can be procured, or shared between organizations. It is used to analyze polarization states by rotating about its axis (orthogonal to the polarization plane) using precision rotary positioners. The horn should be placed in the far-field of the antenna and on an elevated platform in a relatively clear area to avoid multi-path reflections and beam blockage.

The sun is also a useful reference source that can be used for several aspects of the radar calibration process. Its usefulness arises also from the fact that it can be observed from most places on the Earth on a regular basis (except at very high latitudes, both North and South). It can be treated as an un-polarized standard noise source whose position at any time from a given location on Earth can be precisely predicted. The solar flux incident on the surface of the Earth is generally non-polarized, and varies from 100 to 300 solar flux units (an SFU is defined as $1 \times 10^{-22} \text{ W Hz}^{-1} \text{ m}^{-2}$). Measurements are made available from several solar observatories such as the Solar Environment Center or Dominion Radio Astrophysical Observatory at Penticton, BC, Canada at 10.7 GHz and can be scaled to other frequencies, such as C and X band. At 10 cm wavelength the (microwave) sun is approximately 7% larger than the optical sun. One should be also aware that the “microwave center” of the sun does not always lie at the center of the visible disk. Thus use of the sun to evaluate antenna pointing accuracy can encounter difficulties (except at very low latitudes where east- and west-pointing measurements can be averaged).

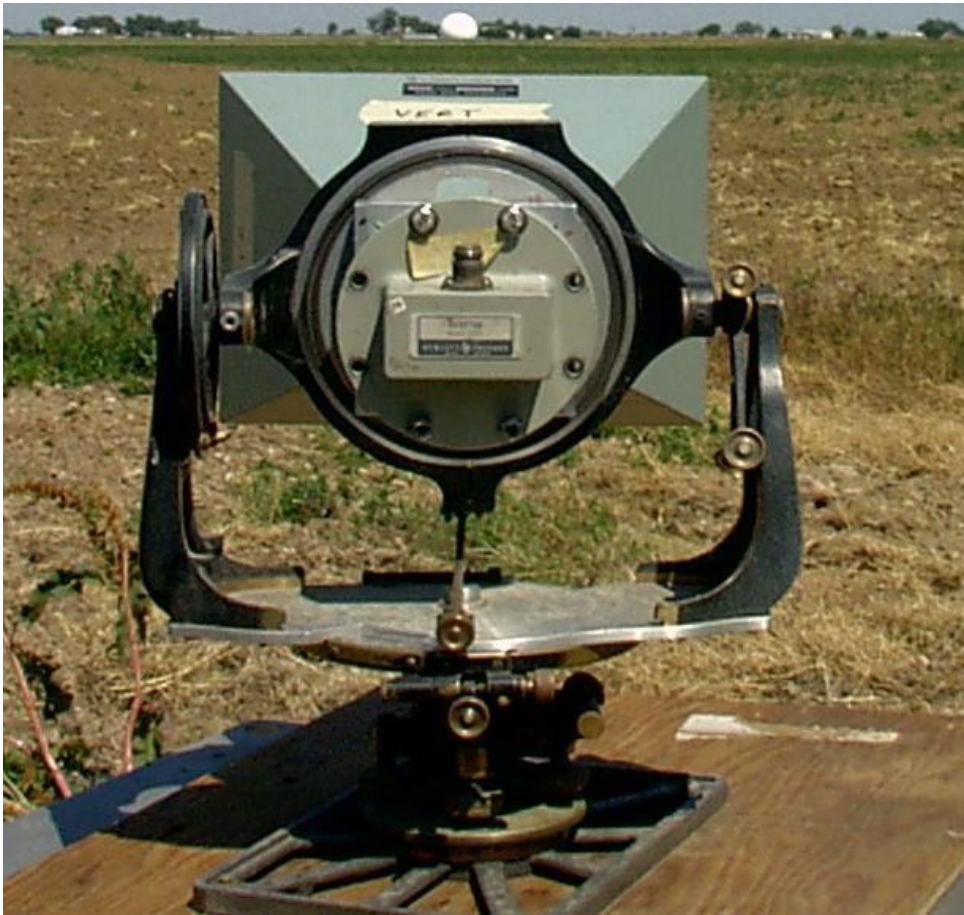


Figure 3: A pyramidal standard gain horn antenna at CSU-CHILL facility.

Most weather radar manufacturers provide a utility, that will be henceforth referred to as solar scan utility (SSU), that can automatically perform some calibration applications based on the sun, such as the determination of antenna pointing and estimation of two dimensional solar observations that are referred as sun scans.

The following subsections describe the basic measurements that can be carried out during scheduled maintenance operations. Keeping track of measurements is of central importance and regular sun scans go a long way in this aspect. The appendix of the document contains tables that can be used for documentation purposes.

2.1 TRANSMITTER MEASUREMENTS

To estimate the equivalent radar reflectivity factor Z_e from \bar{P}_r , using the radar equation (5), transmit parameters, such as peak power P_t , transmit wavelength λ and pulse duration τ are supposed to be known. However, other elements characterizing the transmit signal that are not explicitly mentioned in the radar equation (such as the pulse shape) should also be characterized. These can be measured and monitored over time for diagnostic purposes, because they affect some parameters that explicitly appear in equation (5) that describes the received power. The following subsections describe which are the relevant transmit parameters that may be monitored and some methodologies to measure their performance.

2.1.1 Transmitted wavelength (frequency)

The parameter λ appearing in (5) is normally determined by measuring the transmit frequency f and using the conversion $\lambda = c/f$; alternatively, this relationship can be used to rewrite (5) in terms of f . Frequency measurements can be made with electronic frequency counters or spectrum analyzers (SA) or with tunable-cavity instruments. In systems with power-amplifier-type transmitters such as klystrons or traveling-wave tubes the frequency is usually established by a precision oscillator arrangement and tends to be quite stable. For systems with magnetron transmitters, the transmitted frequency can fluctuate because of the influence of different environmental conditions, particularly as far as the operating temperature is concerned. To limit the influence of these fluctuations, the transmitter needs to work in stabilized environmental conditions. Automatic frequency control (AFC) systems that follow changes in the transmitter frequency to readjust the receiver can be helpful to detect and compensate variation within a narrow range. In the installation phase and during maintenance operations, using a spectrum analyzer, investigations on possible influence of operating temperature on transmit frequency should be done.

2.1.2 Transmit pulse: power, duration, shape, spectrum, and repetition frequencies

Most meteorological radars operate with pulsed transmissions. Characteristics of the actual transmitted pulse have a major influence on system performance. Several characteristics of the transmit pulse are explicitly included in (5) or influence it indirectly. Power measuring (and other) instruments are limited in both the amount of average power and the amount of peak power that can be safely tolerated. Therefore, a directional coupler, and often additional attenuators, are required to couple only a small fraction of the transmitter power and provide a

safe drive level to protect whatever test instrument (such as power meters, spectrum analyzers, or detectors) is used to measure the pulse characteristics.

Peak transmitted power P_t and pulse duration τ are explicitly used in the radar equation (5) and in principle both must be determined. Many different terms are used when talking about power. Peak power is the maximum instantaneous power, though in applications such as (5) what is implied is the average over one complete RF cycle at the peak of the pulse envelope; average power is the power averaged over the complete waveform time of the radar. For pulsed radar with an ideal rectangular pulse shape, this is the product of peak power and the duty cycle (ratio of the “on” time to the total pulse repetition interval). Most typical RF and microwave power meters are average power meters, but average-power data can readily be used in the calibration process. The product of the peak power P_t and the pulse duration τ is the pulse energy, and the product of that with the pulse repetition frequency PRF is the average power P_{av} . It is the *product* $P_t \tau$ that appears in equations such as (5), so one can merely divide a measured value of P_{av} by PRF to obtain the product value $P_t \tau$, without need to determine values of those parameters separately. Using average power measurements is therefore a common method for characterizing the power of a radar waveform that is fairly simple to perform. Within the “weather radar equation”, the factors peak power and pulse duration appear as a product, and therefore, knowing the average power is sufficient. This approach has the added advantage that, if the pulse envelope is not perfectly rectangular (as is usually the case) the measurement of pulse energy is still correct, while difficulties in determining P_t and τ separately may lead to errors in the calibration. This implies that “simple monitoring” of average transmitted power measurements in the calibration is very effective. This will be further discussed towards the end, when discussing automatic calibration.

Routine measurements of transmitter power are sometimes done in terms of peak power with peak-reading RF power meters. However, in the case of irregularities in or changes to the waveforms, or in the presence of the magnetron frequency drifts, the ratio between peak and average power (i.e., the duty cycle) may vary as well. Referring to the considerations above, the practice of measuring average transmitted power value that can be implemented routinely is recommended as a good diagnostic tool.

The pulse duration τ that appears in (5) would be easy to determine if the pulse envelope were perfectly rectangular, but otherwise is not related in any simple way to the pulse shape (See Figure 4 for examples of pulse shapes). Using a digital oscilloscope and detector, one can observe and record the shape of the pulse envelope in time. In such a case the pulse duration is usually defined as the width of the pulse at the instant when the signal is either one half or (better) 70.7% of signal maximum amplitude. However, the product of this estimate of τ and

the measurement of peak power P_t may or may not provide a good approximation of the pulse energy.

A sample of the transmitted signal can be analyzed through a Spectrum Analyzer provided that a calibrated coupler and attenuators as necessary to reduce the signal level into the SA are used. The SA output indicates the center frequency of the transmitted signal, and the frequency and level of side lobes in the spectrum.

To estimate the actual pulse repetition frequencies measurements performed with a basic oscilloscope are sufficient.

2.1.3 Transmitter measurements summary

The appendix provides a reference form that summarizes the measurements of the transmitter sub-system power over a calibration exercise. Records should report date, instrument used for measurement, and average/peak power values (for both channels in a polarimetric or dual-wavelength system). Use of the same instruments that are routinely sent to calibration labs is strongly recommended. The record of when the test instruments are sent for calibration is a good practice.



Figure 4: Different shapes of pulses with different durations (Polar 55C radar, CNR, Italy).

2.2 ANTENNA MEASUREMENTS

Calibration of the antenna performance includes the characterization of both mechanical performance and the electromagnetic properties.

2.2.1 Antenna pointing

Currently most weather radars rely on mechanical drive systems to steer the beam. The accuracy in positioning the antenna will determine the accuracy with which the volume of the precipitation samples can be characterized. This is critical in applications where cross measurements from different radars (at different frequencies or in regions of overlapping) are performed. Accurate positioning of the radar antenna is necessary for properly georeferencing radar measurements. Analysis of the antenna pointing angles can be accomplished by combining different methodologies that include the use of very precise angle measurement devices and specifically designed solar scans. These devices can include a classical gunner's quadrant (GQ), a precision clinometer, or a modern laser pointing device. The angle measurement devices allow for checking linearity of any positioning error while the solar scans are intended to determine the relationship between the indicated azimuth or elevation angle and the true orientation of the beam axis.

Modern radar processors typically provide a Solar Scan Utility that allows for periodic check of the antenna pointing accuracy. In order to accomplish that, the typical SSU runs a sector scan across the sun, covering specified azimuth and elevation sectors centered on the "expected" sun position, with elevation step sizes that can be specified by a user. The sun cannot be considered a point target and therefore effects of its finite size must be taken into account by the SSU processing. Moreover, the size of the "microwave sun" differs from that at visible wavelengths and is also slightly different between frequency bands (such as S to K_a band). If the SSU runs the scan in typical raster mode, with alternating clockwise and counterclockwise traverses on successive elevation steps, any significant backlash in the azimuth data system linkage will blur the solar image and increase the uncertainty in comparing the antenna pointing-angle data with the known sun position. Consequently the azimuth backlash tests discussed in Secs. 2.2.1.3 or 2.2.1.4 should be conducted prior to use of the SSU. Then the SSU fits a two-dimensional paraboloid to a contour plot of the solar return signal, and provides a value of the peak solar "signal" intensity along with estimates of the antenna orientation errors in azimuth and elevation as well as the beamwidths. The SSU requires a minimum intervention of the operator and can be run numerous times over the course of a calibration work or during routine radar operations in absence of precipitation.

Although the solar scan can be done almost all the days, the use of solar scans for antenna pointing purposes can be limited depending on the radar frequency, the latitude of the radar and the day when the SSU is run. For example, the antennas of high-frequency radars may be too small to collect a solar signal with sufficient SNR; moreover, microwave thermal emission from any intervening clouds can become a concern. Comparison of sun position to antenna pointing SSU data can be compromised by atmospheric refraction effects that could be relevant at low elevation angles. Therefore the use of sectors where the sun is too low should be avoided because of potential refraction problems. Radars in tropical latitudes have the ability to observe the sun over a wide range of angles, in order to characterize positioning accuracy over a large range of elevation and azimuth angles. However, data quality at azimuths around 0 deg or 180 deg may be poor because the sun will be at high elevation angles where it subtends a wide azimuth sector. At high latitudes the range of elevation angles accessible in solar scans will be limited.

A difference may be observed between morning (“sun rising”) and afternoon (“sun setting”) pointing-error values; if the pedestal is truly level (this should be checked as outlined in the next section), such a difference is probably related to some displacement of the “microwave center” of the sun from the center of the visible disk. The ephemeris data used by the SSU as a reference for determining any orientation errors are based on the location of that center. At latitudes near the equator any such displacement would contribute error increments of roughly equal magnitude but opposite sign in data from eastward- and westward-looking directions. Comparison of the error data from morning and afternoon sun scans therefore highlights any center-displacement effect, and averaging the two would then indicate how to correct the orientation-angle values. Unfortunately, this capability degrades as one moves away from the equator, and careful attention to the status of solar activity and repetition of the scans over an interval of time become necessary.

2.2.1.1 Elevation Data

For elevation (EL) angle data, a combination of an angle measurement device (such as a gunner’s quadrant or clinometer) and solar scans can be used. In what follows a GQ (Figure 5) will be used for purposes of illustration, but any clinometer with precision of order 0.01 deg could be used. The GQ data provide accurate measurements of angle increments from some reference, such as the plumb position of the antenna reflector, and allow for characterizing any nonlinearity in the angle data conversion device used by the radar. Such a nonlinearity can make it difficult to extend the absolute angle data calibration over the full range of angles. Solar scans can then provide absolute values of pointing angles, allowing for compensation for any boresight error in the antenna.



Figure 5: A gunner’s quadrant measurement on a flat surface being made by one of the authors (PLS) at CSU-CHILL radar facility.

The first step of elevation pointing verification is to assess the precision of the antenna pedestal leveling. This can be accomplished using a GQ mounted on the back of the antenna support structure. A 360-degree azimuth rotation of the antenna, with a fixed elevation, can show peak-to-peak variation of the elevation angle measured by the GQ. For a well-leveled pedestal, this variation should be of the order of 0.04 deg or less (Figure 6).

Once the leveling is assessed, and corrected if necessary, the antenna can be moved, in a fixed azimuth, through a range of elevation angles. Comparisons of EL angle increments (with respect to a reference such as a plumb line) indicated in the RSP output with angle increments determined from the GQ (used as true reference) can reveal any nonlinearities in the angle data indications. These measurements should be performed with antenna movement in both up and down directions; any differences in measurements between the two directions reveal both anomalies in the angle data or evidence of backlash.

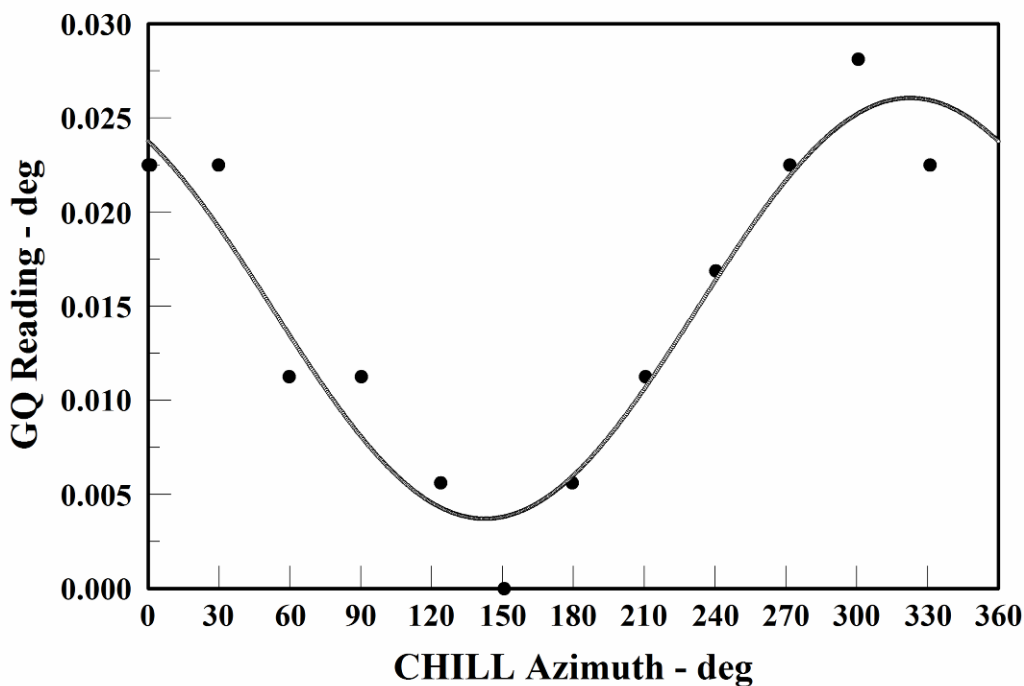


Figure 6: Example of gunner's quadrant (GQ) data checking the leveling of the CSU-CHILL antenna pedestal; the GQ can be read to a precision of 0.005 deg, and the 0.01 deg amplitude of the fitted sinusoid indicates that the pedestal is level to within about 0.01 deg. (The data offset from zero here is of no consequence; the antenna structure need not be at zero elevation during the antenna rotation in azimuth.).

Figure 7 represents an example plot of the difference between elevation angle increments (from an approximately plumb antenna) measured by the RSP and elevation angle increment determined by the GQ. The CSU-CHILL antenna uses digital shaft position encoders; a slight non-linearity, amounting to less than 0.1 deg over the full 45 deg range of the plot, is apparent. Comparison of the upward and downward data shows no evidence of any significant backlash.

Some antenna angle-data systems that derive the position data from synchros and employ a synchro-to-digital conversion process for further processing exhibit more substantial nonlinearities. Figure 8 shows an example from the NASA KPol S-band radar at Kwajalein Atoll (Republic of the Marshall Islands); note that the range of the ordinate in this figure is three times that in Figure 7. Here there is evidence of much greater nonlinearity as well as significant backlash.

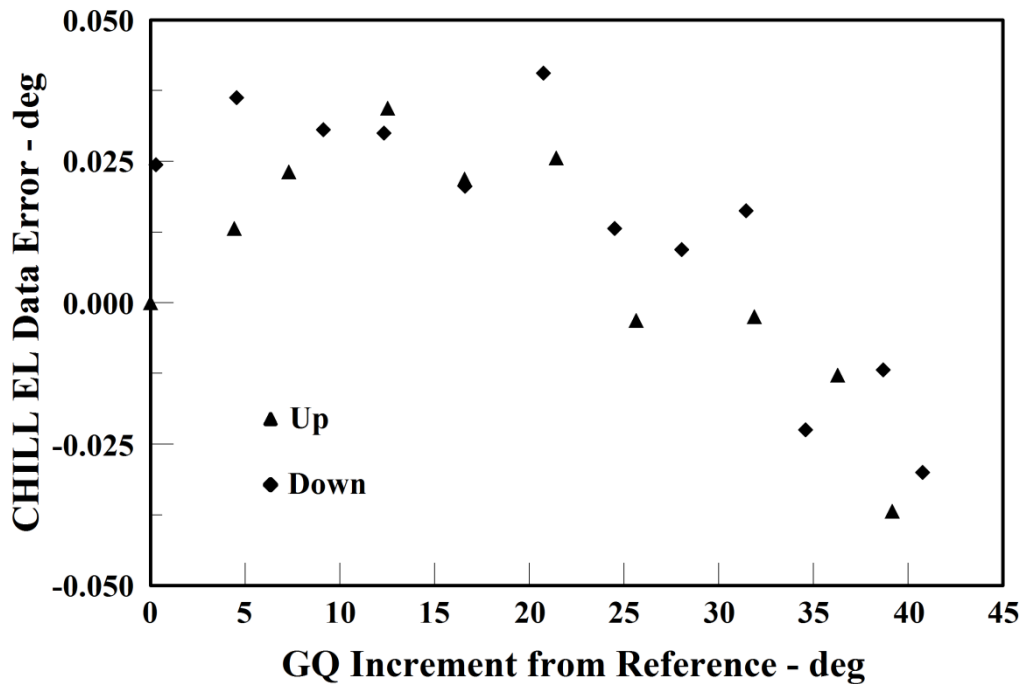


Figure 7: Plot of errors in the indicated elevation angle increment (from an approximately plumb starting orientation) versus the actual increments measured with a gunner’s quadrant. No easy access is available to establish a plumb orientation of the CSU-CHILL antenna, so the reference orientation was an indicated elevation angle of 0.01 deg (One high-elevation data point, lying almost 0.3 deg away from the others, was omitted from the plot as probably due to a reading error.)

The backlash problem was traced to a defective anti-backlash gear in the elevation synchro linkage; replacement of the gear reduced the indicated backlash to about the same order as the typical 0.03 deg uncertainty in synchro data. It is more difficult to deal with the nonlinearity problem, because no simple linear (additive) adjustment to the elevation data can correct the error at all elevation angles.

2.2.1.2 Elevation Orientation

When the antenna is plumb, the beam axis may not actually point to zero elevation because of some boresight error in the antenna alignment. Thus checking the absolute accuracy of the elevation data requires an external reference; with the caveats discussed in Sect. 2.2.1, the sun usually provides the most suitable such reference. Ephemeris data provide accurate sun position information, and solar scans at elevation angles high enough to avoid ground reflection and atmospheric refraction problems provide the data needed to evaluate, and if

necessary adjust, the radar system elevation data. Solar scans with the above-mentioned SSUs can provide the necessary comparison data, but with a little practice the data can also be acquired manually for suitably-configured radar systems. Figure 9 shows an example plot of nonlinear elevation data errors determined from solar scans with an SSU. The indicated nonlinearity over the plotted range is more than 1/3 deg, but as suggested below the data below about sun EL 12-15 deg are probably affected by atmospheric refraction processes. No backlash information can be inferred here from comparison of the sun rising (eastward-looking) and sun setting (westward-looking) data, because all the SSU scans start below the sun elevation and scan upward.

Plots such as Figure 8 and Figure 9 indicate that the errors in the elevation data cannot be reduced to zero at all elevation angles by a simple fixed additive adjustment. Fitting a curve (a sinusoid is the most likely function) to the data would provide a means for correcting the elevation data.

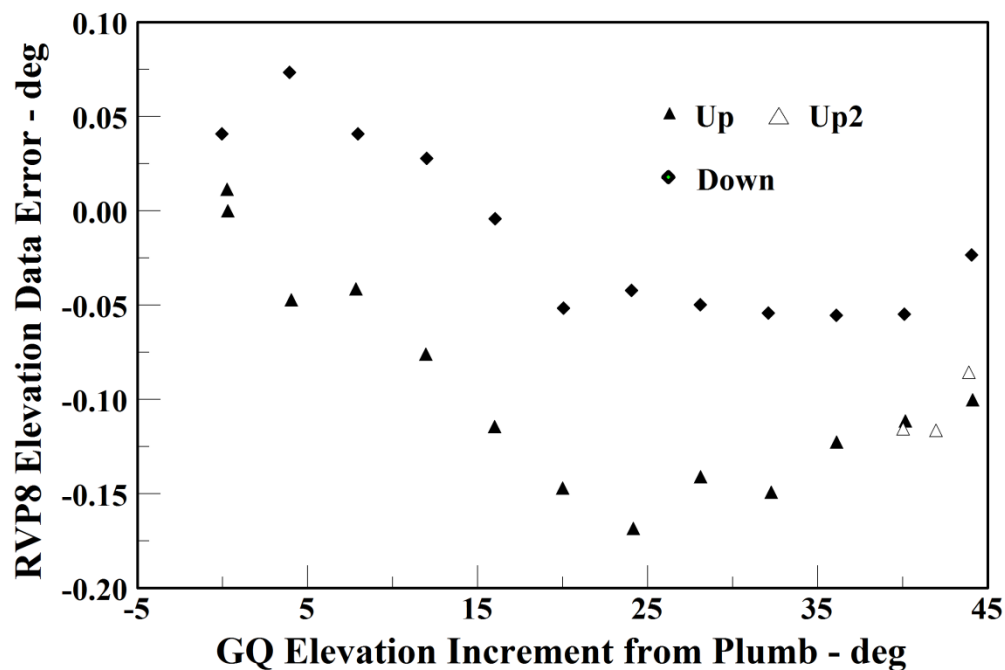


Figure 8: Example plot of error in indicated elevation angle increment (from plumb antenna) vs. true angle increment measured with gunner's quadrant (GQ); points denoted by open triangles represent repeated measurements.

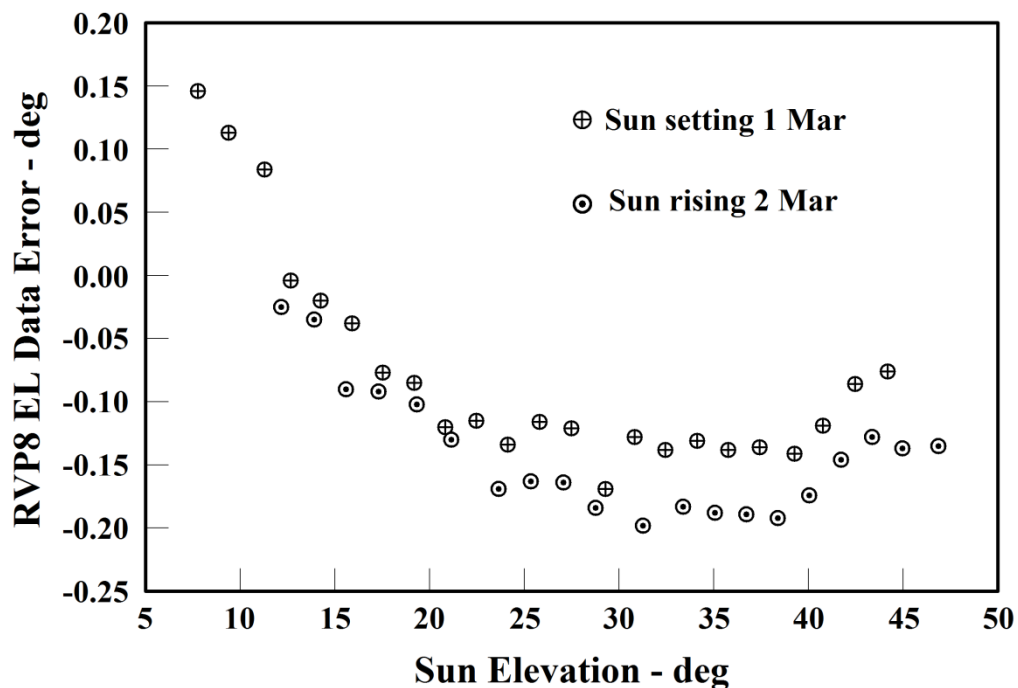


Figure 9: Example plot of nonlinear elevation data errors, as determined from solar scans with an SSU.

In systems where only an additive adjustment (an “elevation offset” correction) is available, the best that can be done is to either center the errors around zero or drive them to zero at some specified elevation angle. In weather radar applications the low-angle data are usually most important, while data from high elevation angles come from nearer the radar and hence are subject to smaller errors in actual vertical distances. Consequently a plausible approach is to make an offset adjustment that yields near-zero errors at zero elevation and accept the fact that the angle errors will be greater at higher elevation angles.

To do this, one first overlays the solar-scan of Figure 9 and GQ elevation-error data on a common plot, as in Figure 10. The GQ-based relative errors are (essentially by definition) zero at the reference position (at or near zero elevation, usually plumb), and are independent of any additive adjustment to the EL data values. To make the solar-scan absolute errors also zero at the reference position, one merely adds an adjustment to the elevation data that moves the solar-scan data up or down the plot until they overlap the GQ data.

The plots may not be parallel over the full EL range. If they are parallel only for high elevation angles, the likely explanation is the influence of atmospheric refraction effects that

affect SSU outcomes at lower EL angles. This behavior is evident in Figure 10 below about 15 deg elevation. To avoid this influence, it is necessary to work with data in the EL range where the plots appear to be fairly parallel. The offset between the two sets of points can be assumed to be the needed elevation data offset. Figure 10 is based on solar-scan data obtained after an initial adjustment to the EL data; consideration of the portion of the plot above 15 deg elevation suggests that a further adjustment to move the solar-scan data points a few hundredths of a degree downward would be in order.

In summary, the EL offset adjustment should make the SSU and GQ plots overlap. Any offset adjustment made to the EL data should be rechecked with a new set of solar scans. Long experience with trying to decide the proper sense (positive or negative) of any adjustment to be made indicates that it is usually quicker to just choose one and check to verify both the sense and magnitude of the adjustment. Repeating the solar-scan measurements under different conditions could highlight the effect of changes in the refraction index in different days.

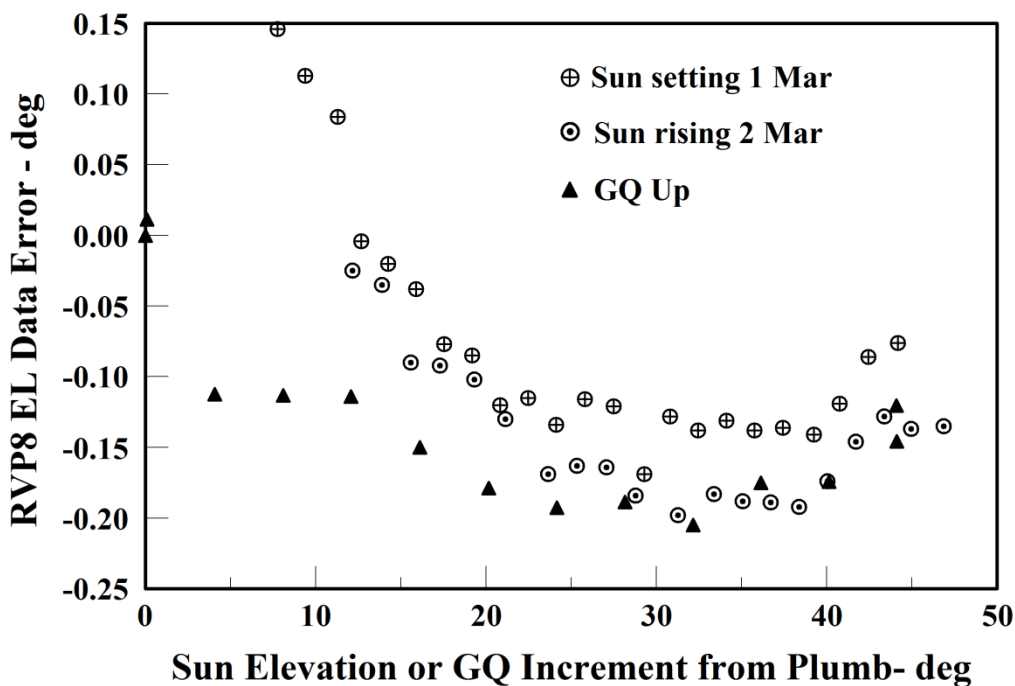


Figure 10: Example plot of solar-scan (absolute) and GQ (relative) elevation-error data overlaid on a common plot. Only the GQ “upward” data are included here because the SSU employed for the solar scans works upward from below the sun.

2.2.1.3 Azimuth orientation

For the azimuth data there is no independent reference device corresponding to the GQ. Consequently checking the azimuth orientation cannot rely on the difference between data from such a device and the antenna azimuth (AZ) data to estimate relative errors. Therefore, azimuth data verification has to rely only on absolute-error data collected via the SSU. Other point-target observations (employing such things as balloon-borne spheres or corner reflectors) are sometimes used for this purpose. Solar observations can be hampered by the limited range of azimuth angles that can be satisfactorily examined with SSU scans.

As previously stated, the SSU itself, or the operator, should limit the azimuth sector considered, avoiding the use of sectors where the sun is too low because of potential atmospheric refraction problems (though such problems have lesser effect on the AZ data). Sectors where the sun is so high that the distinction between AZ and EL angles becomes blurred should also be avoided because it is difficult to get good angle error values. Nevertheless, if the azimuth data system exhibits nonlinearity similar to that illustrated in Figs. 8-10 solar data from a sector wide enough to permit fitting a sinusoid to a plot of the AZ data error vs. AZ angle are desirable.

For radar systems in which the GQ elevation-data check shows reasonable linearity (as in Figure 7) and the AZ data come from a similar transducer (e.g. a digital shaft encoder), it is reasonable to assume that a simple additive adjustment should suffice to correct any errors in the AZ data. For such systems the AZ data errors indicated by solar scans should be essentially independent of the AZ angle unless the “microwave center” of the sun is displaced. In that case averaging of errors found for different AZ directions may yield a reasonable estimate of any required offset to the AZ data (especially at low latitudes). It is recommended to repeat solar-scan experiments in different periods of the year, with optimal AZ sectors for performing the SSU. Such repeated measurements could show possible displacement of the “microwave center” of the sun from its geometric center.

2.2.1.4 Other antenna backlash measurements

A further application of sun position data that is not included in the usual SSU standard functions is the estimation of backlash in the elevation data linkage by simple recording of a slow RHI sector scan centered on the sun elevation. The azimuth is chosen so that the sun crosses the azimuth at which the RHI sector scan is run. Differences in the EL data error at maximum solar-noise power between ascending and descending scans can indicate any backlash.

Similar estimation of backlash can be obtained with a standard gain horn situated in the far field of the antenna, as for the antenna measurements discussed in Sect. 2.2.2. Azimuth traverses in both clockwise and counterclockwise directions, while receiving a signal radiated from the standard-gain horn, provide data to assess any backlash in the azimuth data chain (see Figure 11). This can also be done for elevation, by upward and downward RHIs, though the downward scans through low elevation angles require some care.

2.2.2 Antenna beam pattern measurements

Antenna performance is critical to every radar system. The angular resolution of the antenna appears in (5) as φ_l and θ_l , the half-power widths of the antenna radiation pattern (i.e. the -3 dB beamwidth) that for a radar antenna at S-, C- or X band is typically of the order of 1 degree. Antenna beam patterns are usually measured at the test range by the antenna manufacturer. The beam pattern and beamwidth should not change with time, unless there was an incident with the antenna such as mechanical shock, or fatigue, but periodical field measurements of the antenna pattern can indicate some variations in the performance of the system.

The antenna beam pattern measurements can typically be performed on site by using:

1. An external device. In particular:
 - a. by transmitting the radar signal to a calibrated receiving antenna and microwave power meter located in the far field (distance greater than $2d/\lambda^2$, where d is the geometric diameter of the antenna), and elevated enough to make interference from ground reflections and multipath effects negligible;
 - b. by returning a signal from a source and calibrated antenna in a similar remote location to the radar receiver.
2. The SSU, assuming the sun as an external known radiation source.

Unless automatic means of simultaneously recording both antenna position and received-signal data are available, method 1.a is only practical for limited purposes such as determining the antenna 3 dB beamwidths. The second method has the obvious advantage of a simpler setup. However, the signal to noise ratio achievable using the sun is not sufficient to detect sidelobe levels. Using the method 1.b, beam patterns are obtained by transmitting a CW signal from a distance sufficient to be in far field conditions, and recording the signal received by the radar as the antenna scans across the location of the source. To this purpose, a microwave signal generator can be used with a standard-gain horn to radiate the signal.

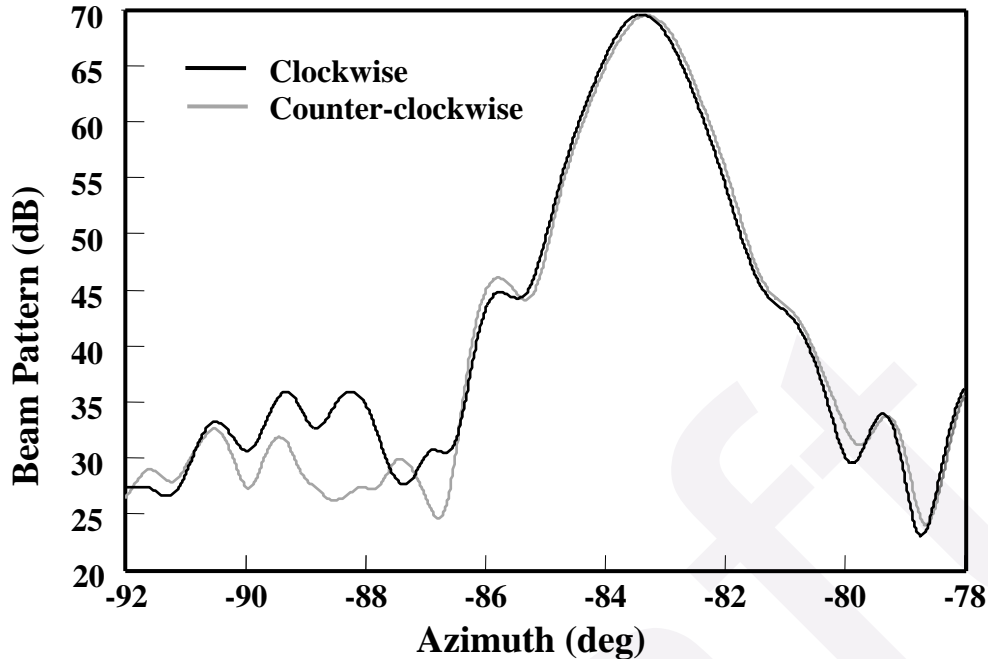


Figure 11: Example plot of data from clockwise and counter-clockwise traverses, at a fixed elevation angle, across the location of a standard-gain horn in the far field radiating a CW signal. The offset between the two curves indicates backlash of 0.09 deg in the azimuth data linkage (CSU-CHILL radar).

Prior to making scans the quality of the horn site should be validated by moving the horn slowly up and down and noting any variation in the signal received at the radar; such variation should ideally be no greater than 0.1 or 0.2 dB. To obtain data for constructing a full 3-dimensional (3-D) beam pattern, scans should be performed with azimuth traverses at a series of elevation steps. To assure a proper oversampling, the antenna azimuth scan rate (ω) for such a beam-pattern task should be no faster than given by the equation

$$\omega = \frac{\text{PRF} \times \theta_1}{n.\text{pulses} \times 20} \quad (6)$$

Here $n.\text{pulses}$ denotes the data sample size. If the traverses alternate between clockwise and counter-clockwise for successive elevation steps, data adjustment for any backlash in the AZ data system linkage will be needed.

Additional elevation scans in the vicinity of the location of the source can be performed at finer resolution to better define the elevation beamwidth.

2.2.2.1 3-D Beam Patterns

3-D antenna beam patterns for the H channel can be obtained from scans made with the standard-gain horn radiating an H-polarized signal or with a 45-deg polarized signal. The top left panel in Figure 12 shows an example color plot of the data (normalized to 0 dB on the beam axis) from such H-polarized signal measurements. Note the alignment of the beam axis with the standard-gain horn at about AZ -83.5 deg. The first sidelobe level is about 26 dB down from the on-axis gain of the antenna. The top right panel in Figure 12 shows a similar plot of the H-channel beam pattern derived from a similar raster scan with the horn radiating a 45-deg polarized signal (for the STAR polarization scheme). The first sidelobe level here is indicated as about 25.2 dB down. A full 3-D antenna beam pattern for the V channel can be obtained from a similar scan with the standard-gain horn radiating a V-polarized signal, or from the same 45-deg signal scan if data from both channels are recorded (Some data systems record only Z_h and Z_{dr} , with the range of the latter values inadequate to determine a full V channel beam pattern.) The bottom panel in Figure 12 shows a color plot of the normalized data from a V channel scan of the former type. The first sidelobe level here is about 26 dB down from the on-axis gain of the antenna.

2.2.2.2 Antenna Polarization Patterns

Performing beam-pattern scans with the horn radiating a 45-deg polarized signal (or using H and V polarizations in the case of alternate polarization radar) as described in Sect. 2.2.2.1, polarimetric variables Z_{dr} , ρ_{hv} , and Φ_{dp} can be recorded. It should be stressed that what is determined in this way is the pattern resulting from the antenna-receiver subsystems and the offset thus determined includes both the difference in the antenna receive gain between the two channels and also the difference in receiver sensitivities, and includes any “ Z_{dr} offset” in the data system. However, it takes no account of any differences in the transmit side of the system. Therefore the absolute values have no particular significance. The variations across the main lobe, however, should be less than 0.1 dB to allow the weighting of differential reflectivity for scatterers across the main part of the beam to be reasonably uniform. For such scans, data from traverses close to the ground can involve contamination due to ground reflection, so care is necessary in interpreting the data from the lowest levels.

Co-polar correlation coefficient recorded using CW signals of nearly equal strength coming to each channel from the 45-deg horn, a near-perfect correlation in the main part of the beam pattern would be expected and indicates the quality of the horn location in terms of freedom from ground reflections and multipath effects.

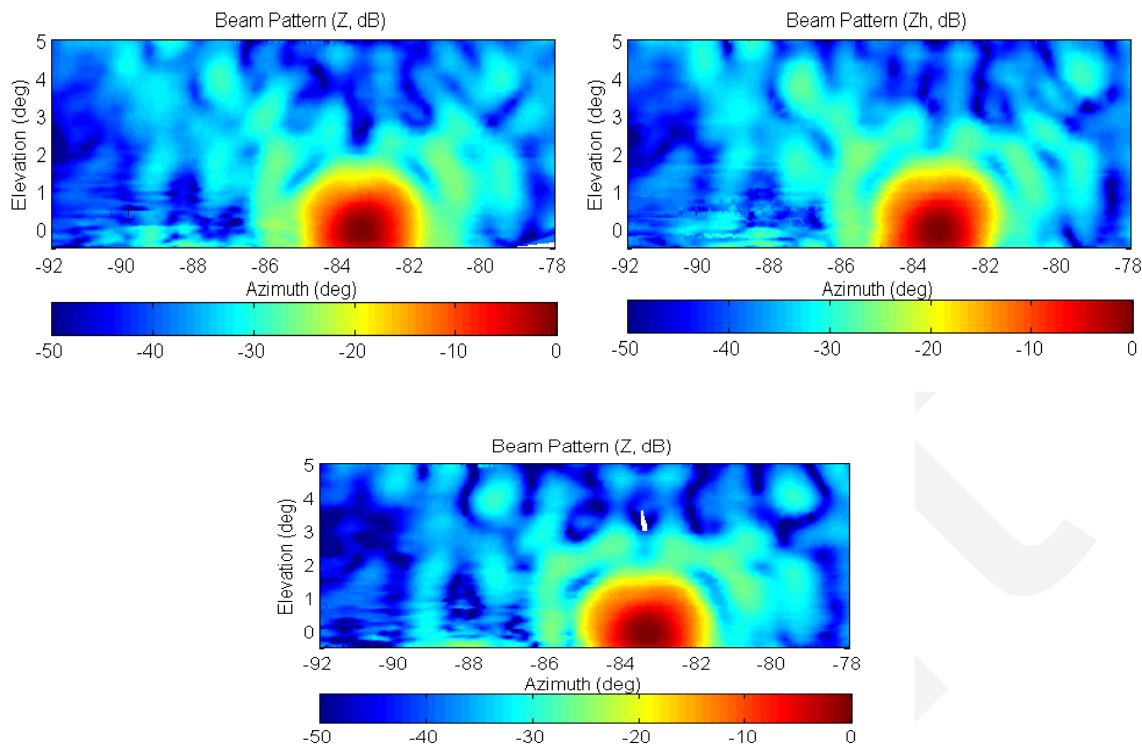


Figure 12: Color plots of antenna beam patterns obtained with the standard-gain horn radiating a test signal. Top: H-channel antenna beam patterns obtained with the horn radiating (left) an H-polarized and (right) a 45-deg- polarized signal. Bottom: corresponding plot of the V-channel antenna beam pattern obtained with the standard-gain horn radiating a V-polarized signal.

Finally, differential phase pattern is mainly useful in indicating the inherent system differential phase (Φ_{dp} at range zero). The differential phase should also be fairly uniform across the main lobe.

2.2.2.3 Antenna beamwidths from principal-plane cuts

Data from principal-plane cuts through the beam axis permit determination of the antenna beamwidths. For example, data from a traverse through the location of the standard-gain horn used to obtain the beam pattern data (e.g. Figure 13), with the elevation of the beam axis at the same elevation as the horn, can be used to determine the azimuth beamwidth. A Gaussian (or parabolic, on semi-log scales) fit to the data points near the beam axis (indicated by dots in the figure) identifies the 3 dB beamwidth in azimuth. If the fit is of the form $y \text{ (dB)} = -a[x \text{ (deg)} - b]^2$ the 3 dB beamwidth will be $2 \times (3/a)^{1/2}$. In Figure 13 the value is 1.04 deg.

To determine antenna beamwidth in EL, data from the same 3D scan patterns can be used. However, to achieve higher precision it is better to run several upward RHI scans with the standard-gain horn radiating. It can be convenient to displace each scan by a small amount in azimuth to assure that at least one would go through, or very near, the horn location.

2.2.2.4 Antenna pattern measurements using the sun

The SSU can also be useful to determine the antenna pattern in the main lobe. As mentioned earlier, the sun can be considered as a standard noise source. Received power density at the antenna can be obtained from observatory S-band solar flux values (adjusted for attenuation by atmospheric gasses) that can be converted to the radar frequency at S-, C-, or X-band frequencies according to published conversion tables (Tapping 2001, eq. 4.1). For antennas with the same gain and receivers with the same bandwidth and noise figure, power collected at the receiver is maximum at S-band, whereas it can be lower by about 4.5 and 8.0 dB at C- and X-band frequencies, respectively. This makes it difficult, at X-band, to get such pattern measurements.

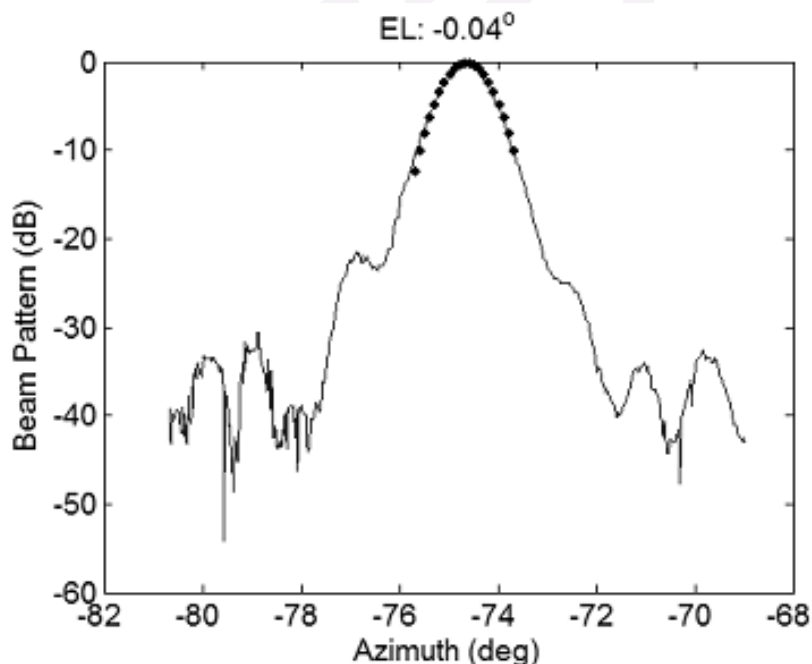


Figure 13: Example of data from an azimuth cut through the antenna beam axis. With these semi-log scales, the parameters of a parabola fit to the points near the axis determine the 3 dB beamwidth.

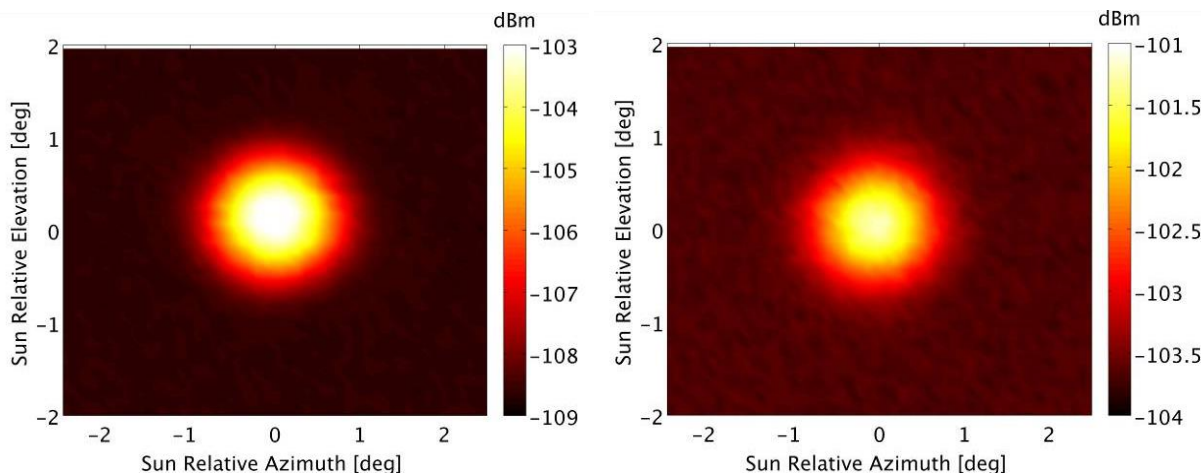


Figure 14: Example of received power pattern (horizontal polarization) obtained via a solar scan with the D3R radar at Ku (left), and Ka band (right).

To obtain accurate results, the SSU should scan the sun slowly, take into account the sun's movement, correct for the size of the solar disk as well as any elevation-angle-dependent atmospheric distortion, and, finally, subtract the receiver noise power. Figure 14 (right) shows an example of received power pattern at horizontal polarization for the NASA D3R radar at Ku (left), and Ka band (right).

2.2.3 Polarization of the transmitted wave

The polarization of the signal radiated from a radar antenna can be obtained from measurements collected with the set up previously described. While the radar transmits its H and then V component (Alternate Polarization scheme) or simultaneous H and V components (STAR scheme), the standard-gain horn is rotated in steps around the line-of-sight axis. At each rotation step the power received by the horn is measured with a power meter. A plot of the power received at the horn as a function of the horn rotation angle, like that of Figure 15, can be obtained. If the radiated signal were linearly-polarized, this received power would exhibit a sharp minimum where the horn polarization is orthogonal to that of the signal. If the signal were circularly-polarized, the received power would not vary as the horn is rotated, while elliptical polarizations yield intermediate variations.

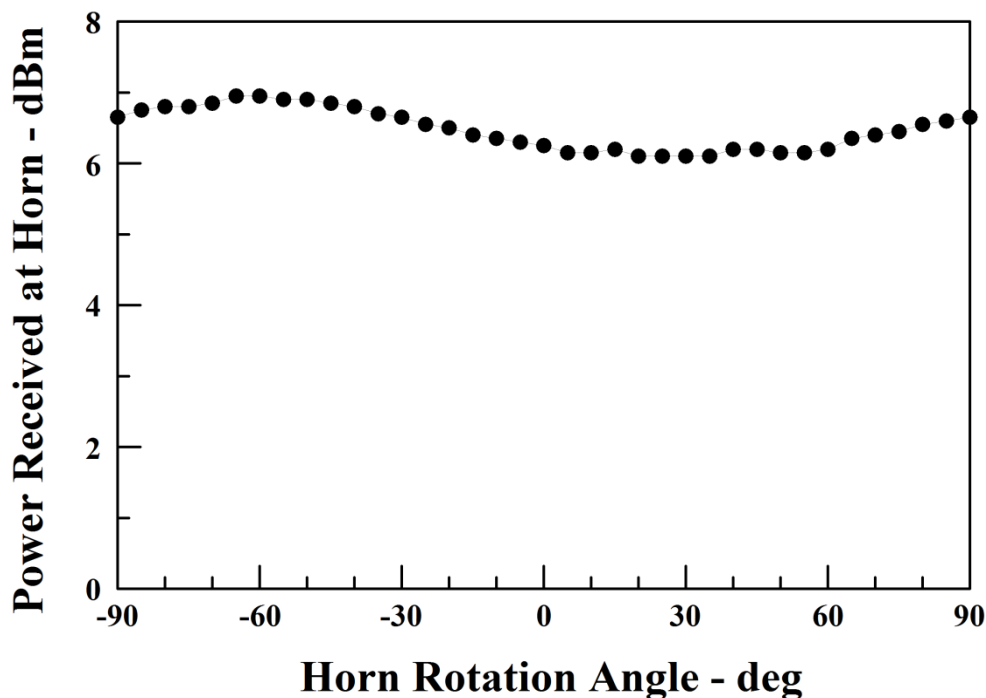


Figure 15: Power received at standard-gain horn as a function of the horn rotation angle, for a case where the polarization of the radiated signal is nearly circular (0 deg indicates vertical polarization for the horn).

The plot in Figure 15, showing a variation that is less than 1 dB in a signal level that ranges between 6 and 7 dBm, indicates that the current polarization of microwaves radiated from this radar antenna is nearly circular.

Figure 16 shows an example plot of power received at the standard gain horn as a function of the horn rotation angle where the variation indicates an actual elliptical polarization.

If desired, the axial ratio for an elliptically polarized signal can be determined by noting the maximum and minimum power levels in a plot like Figure 15. Taking the square root of those values (in power, not dBm, units) yields quantities proportional to the sum and difference, respectively, of the amplitudes of the right- and left-hand circular E-field components of the elliptical signal; the quotient of the sum over the difference is the desired axial ratio. The inclination angle of the ellipse is indicated by the maximum or minimum value in the plot.

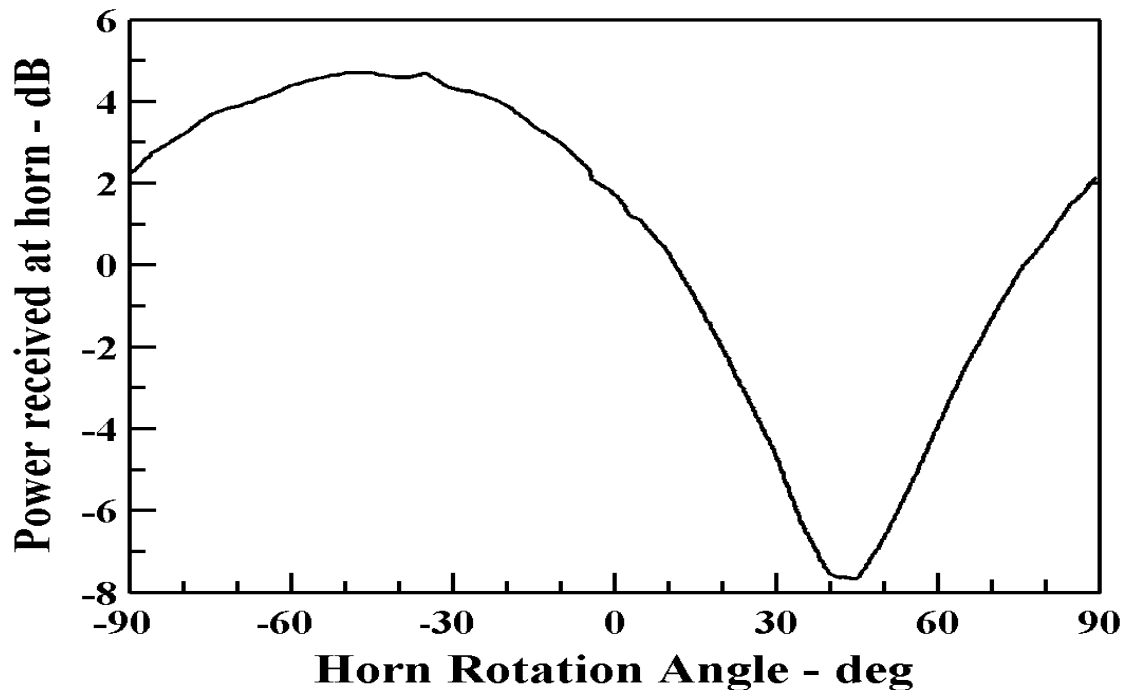


Figure 16: Power received at standard-gain horn as a function of the horn rotation angle, for a case where the polarization of the radiated signal is elliptical. (0 deg indicates vertical polarization for the horn).

2.2.4 Orientation of the antenna H and V Components

Another similar series of measurements using the reciprocal propagation path, with a Signal Generator as the source and the horn as the transmitting antenna, permits verification of the alignment of the H and V components of the antenna pattern. The horn is rotated as before and the H and V components of the signal received recorded to evaluate the orientation of the antenna H and V components. The received H component should exhibit a sharp minimum at the 0-deg horn angle (vertical polarization of the signal from the horn), while the V component should show a sharp minimum at ± 90 deg (horizontal polarization of that signal).

Figure 17 shows an example of results of such measurements. Expanded-scale plots with finer resolution in the horn rotation angle around 0 and ± 90 deg can be useful for detailed verification.

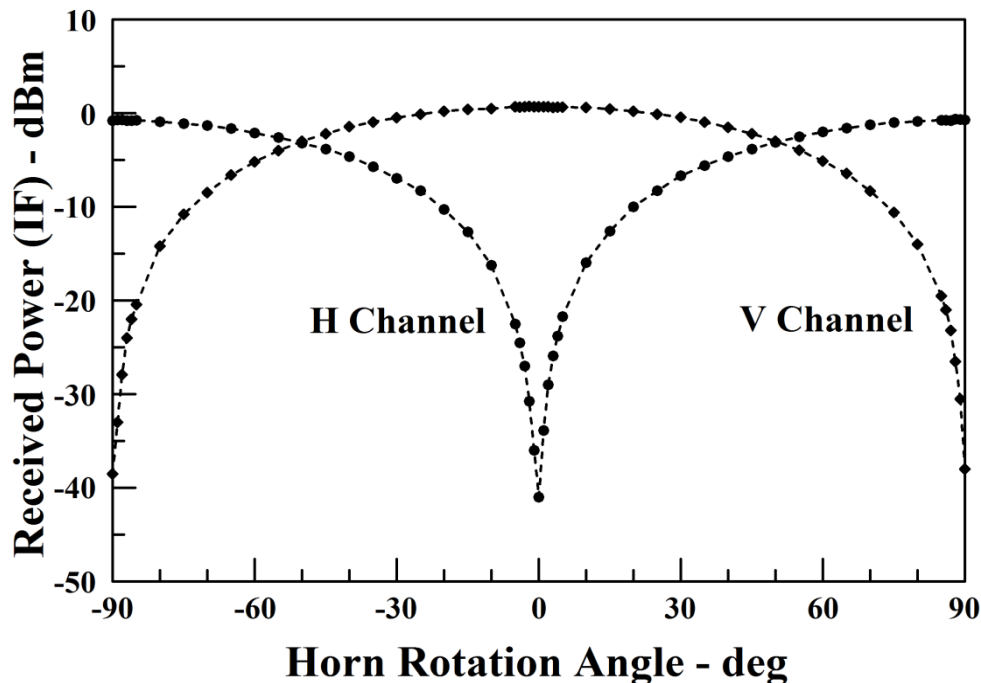


Figure 17: Example plot of results with obtained with a rotated horn transmitting to the radar.

2.2.5 Effective Antenna System Gain

Antenna gain is defined as the maximum radiated power density relative to the power density that would be radiated from an isotropic antenna (it is sometimes referred to as directivity). Antenna gain is usually specified in the logarithmic unit of dBi (i.e. dB relative to an isotropic antenna). The nominal gain of a paraboloidal antenna of physical aperture area A operating at wavelength λ is expressed by equation

$$G_{\text{nom}} = e_a (4\pi A/\lambda^2) = e_a (\pi d/\lambda^2) \quad (7)$$

where d is the diameter of a circular aperture and e_a is the “aperture efficiency.” A typical value of e_a is 0.55; however, to facilitate measurements in the field it is helpful to incorporate losses such as waveguide, mismatch and radome losses into an “effective antenna system gain” G_e (Evans 1990). Under that formulation the effective efficiency may be considerably smaller. The antenna gain may also be polarization-dependent, so that the value could differ for the horizontally- and vertically-polarized signal components.

A common method for evaluating the effective antenna system gain (Evans 1990) uses the pyramidal standard gain horn as a transmitting antenna to send a signal (usually CW) to the receiving radar antenna. The classical Friis transmission formula provides the power received by the radar P_r as

$$P_r = \frac{P_t G_t G_e \lambda^2}{16\pi^2 r^2} \quad (8)$$

where P_t is the power transmitted from the horn (average-power values can be used in both cases); G_e is the effective antenna system gain of the radar, to be determined, while G_t is the gain of the standard gain horn; λ is the radar operating wavelength; and r is the antenna-to-horn distance obtainable from geodetic survey data or distance-measuring instruments. In these measurements the signal generator frequency needs to be tuned to place the IF signal in the receiver at the center of the IF filter passband. The calculated values for effective antenna system gain incorporate all waveguide, mismatch and similar system losses beyond the directional couplers, as well as any radome loss. Results may be recorded using Table 2 and compared with the antenna gain value used in the calibration routine used in the RSP to determine any needed adjustment.

An equivalent measurement of antenna gain can be made using the reciprocal propagation path, with the radar transmitting to the standard-gain horn with an attached microwave power meter situated in the far field of the radar antenna. Here the roles of "transmitted" and "received" in the Friis formula are reversed, but the approaches are otherwise similar. Table 3, similarly to Table 2 allows keeping notes of these measurements. Antenna gain values of the two tables should be similar to each other.

2.2.6 Antenna gain from sun measurements

A way to use solar measurements to obtain antenna gain is described below (Pratte and Ferraro, 1989). As first step, using two noise sources ("hot" and "cold", whose equivalent temperatures are T_h and T_c , respectively) establishes the noise bandwidth B_n (see details in sect. 2.3.3). The background temperature (that of blue-sky, i.e. without pointing to the the sun) is referred to as T_a while the sun is taken into account with an excess temperature T_s . An equation relating the power received from blue-sky can be written as

$$P_a = kT_a B_n G_c \quad (9)$$

while the excess solar received power P_s can be related to T_a and T_s through

$$P_s + P_a = k(T_s + T_a)B_n G_c. \quad (10)$$

These equation can be combined into

$$P_s = kT_s B_n G_c \quad (11)$$

Using equations provided in sect. 2.3.3 concerning noise bandwidth measurements, the excess sun temperature can be expressed as

$$T_s = P_s (T_h - T_c) / (P_h - P_c) \quad (12)$$

Antenna gain can be obtained using an equation relating the effective aperture of the antenna A_e , excess sun temperature T_s , and solar flux density S as

$$A_e = kT_s / S \quad (13)$$

expressing that the effective antenna collecting area is the ratio between the measured solar power density and the incident solar flux close to the antenna. This relation can be expressed in terms of the antenna-system gain G_e instead of A_e as

$$G_e = \frac{4\pi k T_s}{S\lambda^2}. \quad (14)$$

or in logarithmic units,

$$G_e(dB) = Q(dB) - S(dBS) + T_s(dBK) + corr(dB). \quad (15)$$

where $Q(dB) = 10\log_{10}4\pi k/\lambda^2$ and the terms $corr(dB)$ has been added to take into account atmospheric gas attenuation, a 3-dB of polarization correction due to an unpolarized signal to a single polarized receive antenna state, and beamfilling. Solar power density at the antenna can be obtained, as described in 2.2.2.4, from observatory S-band solar flux values properly converted to the radar frequency frequencies. Figure 18 shown an example of weekly estimation of antenna gain performed at CSU-CHILL in 2003. Table 4 shows how to record data of antenna gain solar calibration.

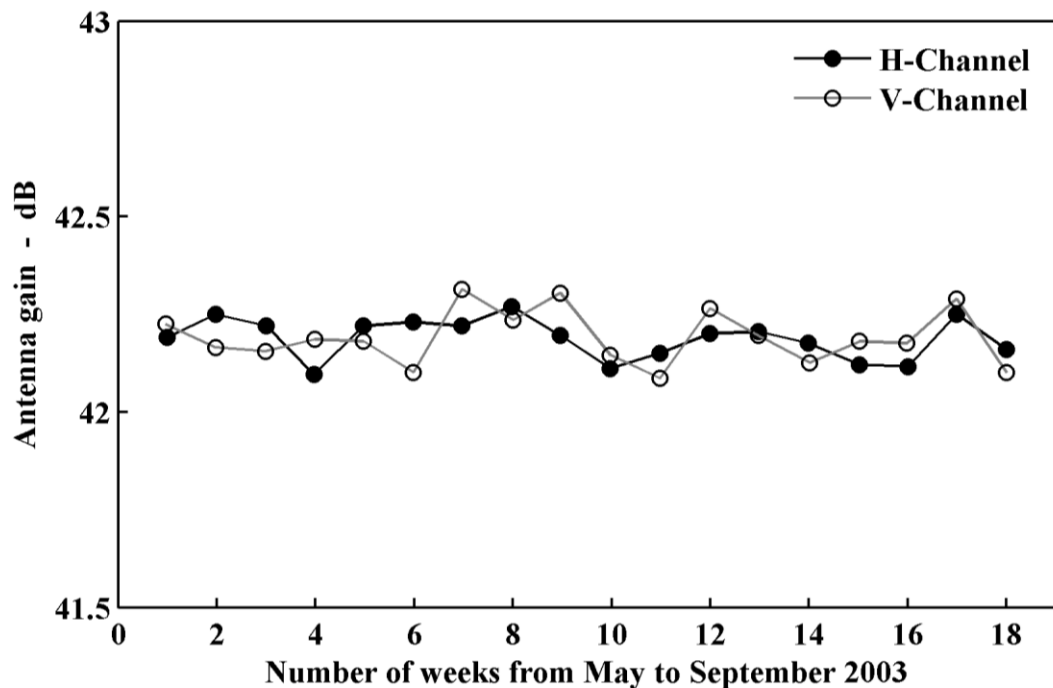


Figure 18: Antenna gain estimated weekly using solar calibration in H and V channels from May to September, 2003 (CSU-CHILL).

2.2.7 Channel cross-talk

The channel cross-talk can be estimated with the standard-gain horn radiating an H (or V) test signal and measuring the power received at radar in both channels. The cross-polarized $H \rightarrow V$ power should be from 35 to 45 dB below the co-polar power received in the H channel when the horn was radiating a horizontally-polarized signal. The converse measurement can be done with the corresponding $V \rightarrow H$ cross-polarized signal level.

2.2.8 Antenna VSWR and other measurements.

Measurements of quantities such as the Voltage Standing Wave Ratio (VSWR) or Return Loss in the antenna system are performed to evaluate mismatch discontinuities in the microwave paths in the antenna. If the power reflected from such discontinuities is excessive, the reflectivity calibration can be affected and other problems such as overheating of the terminations in the circulators may arise; compensation for the reflections with the use of tuning stubs may then be necessary. Three approaches can be useful here; the simplest is to measure the reverse power at bidirectional couplers with a microwave power meter. These data may indicate mismatch problems in the waveguide, but provide no information about the location of the mismatch(es). For that purpose, comparing the envelope shapes and timing of the transmitted pulse and reflected signals in the waveguide (as measured with a crystal detector and oscilloscope) is useful. The most complicated approach involves using a Network Analyzer to examine the reflections in the waveguide run, or segments thereof, as a function of frequency.

2.2.8.1 Return-loss Measurements

The VSWR or return loss can be determined by comparing the reflected power measured at the reverse port of a bidirectional coupler with the transmitted power observed at the forward port. For convenience, these measurements are usually phrased in terms of return-loss values, essentially the logarithm of the ratio of forward to reflected power in the waveguide at the directional coupler location. A return loss of 20 dB corresponds to a 1.22 VSWR, and 17 dB corresponds to a 1.33 VSWR. A return loss of 20 dB or greater is generally regarded as indicating satisfactory matching of the waveguide to the transmitter, though no significant problems may be encountered even with somewhat smaller values. A 20 dB return loss means that 1% of the transmit power is reflected, and 17 dB means 2% reflected. Reciprocity considerations invoke similar reflections of echo signals, for a net 2% or 4% (0.09 or 0.18 dB), respectively, overall loss. With magnetron transmitters higher levels of reflected power may occur when the transmitter is restarted after an extended off time. Such restart is accompanied by slow changes in the frequency as the magnetron warms up.

2.2.8.2 Shapes and Timing of Reflected Signals

The envelopes of the reflections of the transmitted pulses in each channel can be recorded with a suitable oscilloscope using a crystal detector (with attenuator pads as necessary) at the reverse-power ports of the respective directional couplers.

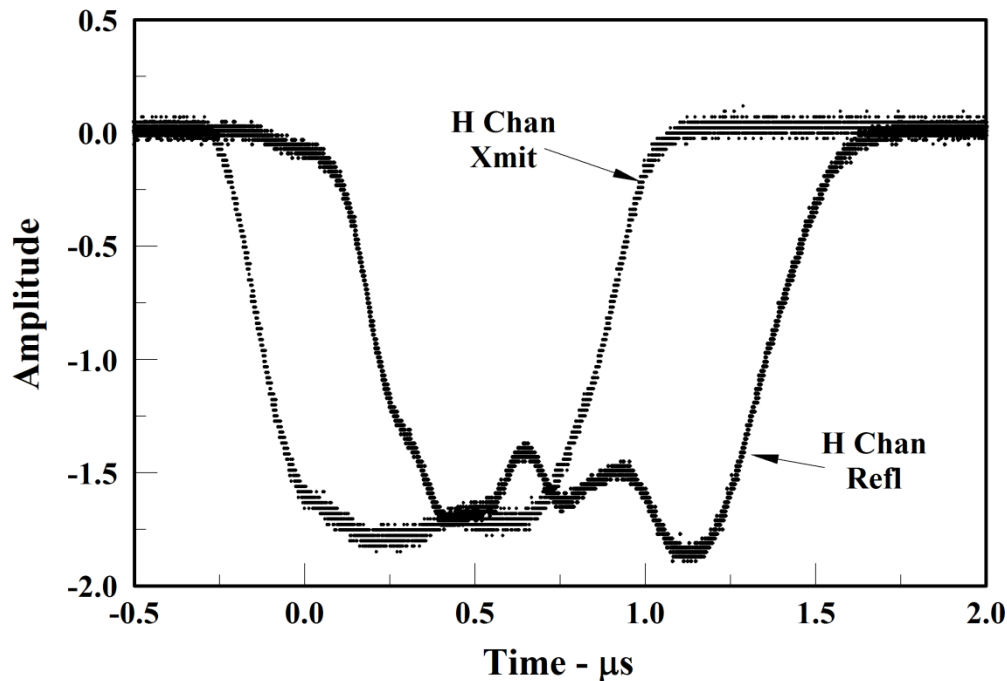


Figure 19: Example plot of detected envelopes of transmitted pulse and reflected signal in the CHILL H channel; signal magnitudes have been adjusted to facilitate timing comparisons.

The cable connecting the detector to the scope should match the output impedance at the coupler port (usually 50 Ω ; RG-58 or equivalent) and be terminated in a matched load at the scope. Signal timing information for comparison with a similar recording of the envelope of the transmitted pulse is obtained by synchronized triggering of the scope, so that the relative timing of the various signals is preserved. Figure 19 shows example results obtained with the CSU-CHILL radar operating in the normal configuration, with a plot of the transmitted pulse envelope overlaid for comparison. The relative amplitude values in such comparisons between transmitted and reflected signals have no significance, because the coupling factors at the ports where the signals were recorded differ. Certain features can be seen in such plots; as is evident, the reflected signal does not necessarily preserve the shape of the transmitted pulse. Here the reflected signal is delayed about 0.34 μs from the transmit pulse; as the group velocity in the WR284 waveguide at the CHILL frequency is about 200 m/ μs , this indicates an origin about 34 m along the waveguide. That places the likely origin at an impedance mismatch in the area of the AZ rotary joint. The reflected signal continues for about 0.49 μs after the end of the transmit pulse, indicating the arrival of a signal originating about 49 m down the guide – likely from a mismatch at the feed horn. Reflections from multiple

mismatch locations along the waveguide arrive back at the coupler at different times, with mutual interference effects modifying the resultant “pulse” shape. Power reflected from significant mismatches can cause difficulties such as overheating of the terminating loads in the circulators. If the return-loss values are not high enough or there are other indications of such problems, it may be possible to isolate the major sources of the reflected signal by breaking into the waveguide at key points (e.g., the elevation rotary joints or the azimuth rotary joint) and affixing a dummy load. Then comparing new return-loss measurements and signal-envelope plots like Figure 19 with the original set can indicate where the principal mismatch reflections are occurring. If tuning stubs are required, they should be installed on the transmitter side of the mismatch closest to the transmitter, and as near as convenient to that mismatch.

2.2.8.3 Network Analyzer Measurements

Interference among reflected-signal components originating from different mismatches along the waveguide can be constructive or destructive when they travel back toward the reverse port of the bidirectional coupler. This means that the net reflected signal will vary with frequency. At 2800 MHz the wavelength in a WR284 waveguide is about 16 cm; thus a waveguide run of 40 m is some 250 wavelengths long. A frequency change of one part in 1000 (less than 3 MHz) would change the wavelength in this guide enough to make the total guide run $250 \pm \frac{1}{4}$ wavelengths. The phase of the signal component reflected from a mismatch at the end of the run (i.e., from the feed horn) would change by 180° at the coupler, and modify the interference of that component with components reflected from other mismatches accordingly. Consequently a shift in the transmitter frequency of just a few MHz may have significant effect on the return loss and any problems associated therewith.

A Network Analyzer can be very useful in investigating such frequency-sensitivity issues. This instrument generates a CW test signal that can be injected into the waveguide through a coax-to-guide adapter and then measures the ratio of the reflected signal power to that of the test signal (hence the negative of the Return Loss). It can be set to sweep over a frequency range (e.g., ± 10 MHz about the radar transmitter frequency) in a series of small steps while recording the ratio as a function of frequency. One should keep in mind that a) such Network Analyzer data are in effect steady-state measurements and take no account of the time delays inherent in pulse propagation along the waveguide; and b) the spectrum of a $1 \mu\text{s}$ radar pulse extends over a range of more than 1 MHz centered on the nominal operating frequency. Thus the return-loss values measured with a Power Meter may correspond in some sense to a kind of weighted average over the single-frequency values provided by the Network Analyzer, but the effect of the time delays also plays an important role.

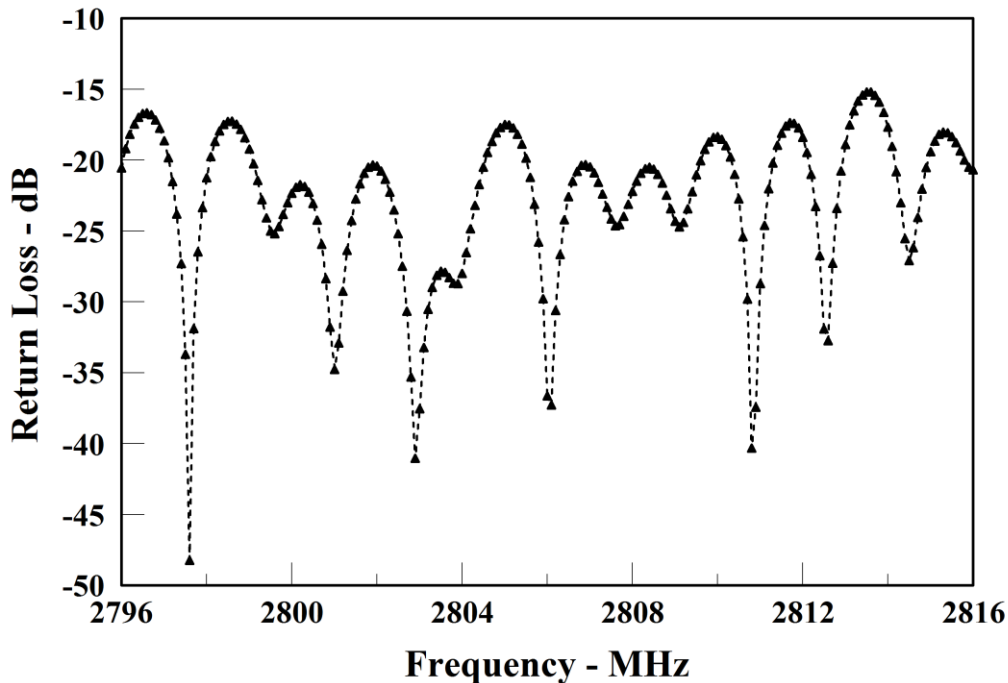


Figure 20: Example of results from a Network Analyzer sweep of the Return Loss (here given with a negative sign) in the waveguide of an S-band radar operating at about 2806 MHz.

Figure 20 shows an example plot of data from a Network Analyzer sweep of the Return Loss in an S-band antenna system. This illustrates the complexity of the effects of frequency variations when multiple sources of mismatch reflections are located along the waveguide run. In this system one might expect significant reflections from the coaxial azimuth rotary joint and the OMT at the feed horn, along with lesser reflections from the elevation rotary joint and other sources such as joints and bends along the guide run. Affixing a matching termination to the waveguide at points just ahead of the suspected mismatch elements can help to isolate the source of any mismatch causing significant reflected-power problems.

2.3 RECEIVER MEASUREMENTS

2.3.1 Receiver Calibration

The advent of fast analog-to-digital converters has enabled the implementation of radar receivers in which the received RF signal, after down-conversion to IF, is then digitized for further processing. Most modern radar digital receiver systems implement a routine that automates the calibration process which determines the digital IF output corresponding to an RF input test signal of increasing level obtained from a signal generator tuned to the transmitted frequency, and injected through a directional coupler. (As noted at the beginning of Sect. 2, it is essential that the directional coupler port used here is the same one used for transmitted power measurements.) The measurements should include a noise-power measurement with the signal generator RF signal turned off. Using different test signal levels, the data are plotted on a log-log display relating IF power at the receiver output to RF power at the directional coupler; the measurements above the system noise level determine relevant calibration parameters for received power and reflectivity calculations. For a linear receiver, this plot should be linear and the slope should be unity (Figure 21). The RSP then stores the appropriate calibration parameters for use during routine operations. For dual polarization radar it is important that such process is applied to separate calibrations for both the H and V receiver channels. The measurements are sensitive to the temperature, especially of the receiver front end (such as low-noise amplifiers) and this calibration should be performed when system warm up is completed. Additional input parameters can be requested by this calibration routine, such as values of antenna gain, the FIR filter loss, other losses and the pulse duration. Results obtained during calibrations can be properly summarized using Table 6. The estimation of these parameters is described below.

2.3.1.1 Intermediate frequency filters and associated loss and bandwidth

a) Filters and digital filter coefficients

The bandwidth of the receiver in a radar system is typically determined by a filter in the IF section, the purpose being to enhance the received signal-to-noise ratio (SNR). In the calibration of the receiver subsystem, IF filters are important because magnitudes of both the signal and the noise output of the subsystem are related to the width of the filter response in the frequency domain; with digital filters the filter coefficients also determine the “front-end gain” or “conversion gain” (from RF to IF power levels) of the receiver (sect. 2.3.1.2).

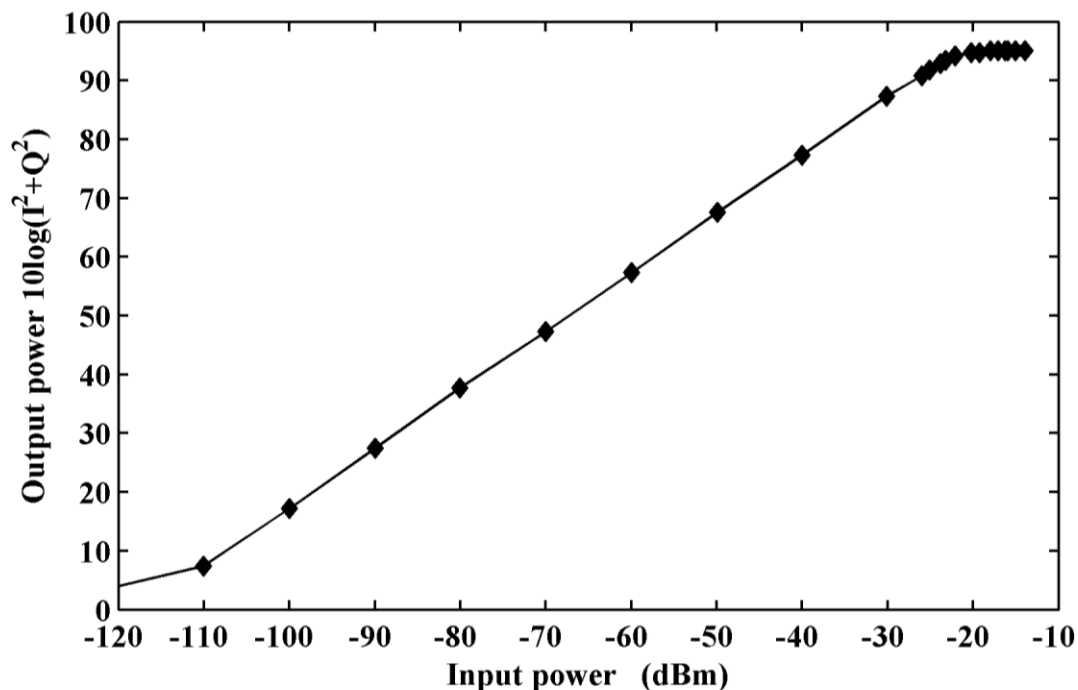


Figure 21: Example of receive calibration plot (CSU-CHILL radar)

Some RSPs let users set the width of the filter response and determine the values of the filter coefficients such that the output power from the filter corresponds to that of a CW IF signal entering the processor. An ideal filter matched to the spectrum of the transmitted signal would yield the highest possible SNR in the receiver; however, in that neighborhood the SNR is not very sensitive to modest increases in the filter bandwidth and somewhat wider bandwidth allows for possible variations in the transmitter frequency or pulse shape. Especially for magnetron systems the width of the filters should take into account possible drift of the transmit frequency (which can be up to several hundred kilohertz); that is driven by several factors, including temperature, age of the magnetron, delays in tuning of the automatic frequency control to the transmitter, and any shift in the pulse repetition frequency.

b) Filter loss

In the context of receivers for weather radars, the term “loss” is defined with respect to infinite bandwidth filters (see Bringi and Chandrasekar 2001 for details). The finite bandwidth of the receive filter determines the loss in received power due to the varying effect of the filter transfer characteristics across the echo spectrum that for weather targets corresponds, on

average, to the transmitter spectrum; the filter rejects part of the spectrum of the received signal, reducing the received power. Once the type of filter response is known (or the filter coefficients are known), the loss due to the filter can be easily calculated. The associated loss factor is calculated in principle by convolving the transmitter spectrum with the filter frequency response characteristics. Values of received power measured during normal weather surveillance operations need to be adjusted to take account of this loss.

In the current days, most of the receivers are digital IF and therefore this filter loss can be calculated from the filter coefficients. Moreover the noise bandwidth (see also Sect. 2.3.3) can be calculated directly from the filter coefficients. The filters' parameters can be stored in the [Table 7](#). Different IF filters can be applied for different pulse configurations.

2.3.1.2 Receiver "front-end" RF-IF conversion gain

As noted in Sect. 2.3.1.1, a proper selection of the coefficients in the digital filter can make the signal processor provide indications of absolute power levels at the input of the IF digitizer. Comparing these values obtained during the receiver calibration to the RF input signal levels at the directional coupler of the receiving channel, and adjusting for the IF filter loss (because the CW test signals are not subject to the filter loss) provides the net RF-to-IF conversion gain (G_c):

$$G_c = \text{IF Noise Level (dBm)} - \text{RF Noise Level (dBm)} + \text{Filter Loss (dB)} \quad (16)$$

This is the gain of the receiver "front end" that incorporates all of the analog components of the receiver, including the gains of the Low-Noise Amplifier (LNA) and the IF amplifier as well as losses in the waveguide, circulator, TR limiter, preselector filter, cables, pads, and mixer. While this may be considered a "detail", it is a good number to note once in a while to make sure nothing is drifting. The value is also useful in determining the receiver noise bandwidth and noise figure (Sect. 2.3.3).

2.3.2 Noise Power Levels

Noise power levels can be measured and stored for each channel, and recorded as in [Table 8](#). The noise power is the lowest power level that appears as part of the receiver calibration. Correction of the echo power received from weather targets is needed to obtain valid measurements of differential reflectivity.

2.3.3 Receiver Noise Bandwidth and Noise Figure

The detection limit of the radar receiver is based on four factors, namely, the noise figure (NF), the quantity kT , where k is Boltzmann's constant and T is the antenna temperature, the noise bandwidth of the system, and the SNR. The noise bandwidth is defined as the value which, when multiplied by the average input noise power per hertz and receiver gain, results in the measured output noise of the system.

This quantity is important in solar calibrations and receiver calibrations using noise sources and is determined by the IF filters. Its value can be determined from two noise output measurements with two noise sources of known, but different, temperatures at the receiver input. The usual choices are the environment temperature (290 K by convention, obtained using a matched termination or attenuator padding amounting to at least 20 dB as a dummy load) and the equivalent noise temperature of a standard Noise Source. The corresponding table to record the measurements is Table 9. The noise bandwidth is then calculated by using two equations of the form

$$P = kTB_n G_c \quad (17)$$

where P is the noise output power at IF from an element of noise temperature T connected at the receiver input, k is Boltzmann's constant, B_n is the noise bandwidth and G_c is the conversion gain of the receiver. The two equations can be solved for the noise bandwidth as

$$B_n = \frac{P_s - P_d}{kT_s G_c} \quad (18)$$

where subscripts s and d indicate measurements made with the Noise Source and with the dummy load in place, respectively. Here T_s represents the excess noise temperature of the source (i.e. a Noise Source with an Excess Noise Ratio of 15 dB corresponds to an excess noise temperature of 8307 K). Finally, the noise figure F_n can then be calculated from

$$F_n = \frac{P_d}{kTB_n G_c}. \quad (19)$$

Obviously all the measurements must be at common reference points. The measurements of the noise power output are normally taken as the IF power available also from RSP. However, it should be noted that the latter calculation may be only an approximation, because the receiver noise power output in the normal operating configuration may differ from that with the dummy load connected; hence the "antenna temperature" may not equal 290 K.

2.4 DUAL POLARIZATION TESTS

The quality of the Z_{dr} data is affected by the balance between the H and V transmit and receive channels. Information about these balances can be obtained from standard gain horn measurements like those discussed in Sect. 2.2.

2.4.1 Transmit Channels

The balance between the H and V transmit channels can be evaluated by comparing signals transmitted by the radar, received with the standard-gain horn and measured using a power meter. Table 10 summarizes these measurements. This measurement can be affected by various factors, including any difference in transmitted power between the two channels, the uncertainties of directional coupler calibrations, or differences between the antenna gain or waveguide loss of the two channels.

2.4.2 Receive Channels

The balance between H and V receive channels can be evaluated by applying equal inputs to the two channels. A suitable test signal transmitted from a Signal Generator and standard-gain horn can be adjusted in polarization by rotating the horn, for example using first H and then V polarization, or with the horn at a 45-deg inclination.

Alternatively, the solar microwave flux, which is non-polarized and therefore comprises equal H and V components, can be recorded (Table 11).

2.5 WAVEGUIDE AND DIRECTIONAL AND DIRECTIONAL COUPLER MEASUREMENTS

2.5.1 Waveguide Losses

Measurements of loss in the different microwave paths are often part of routine maintenance or calibration operations. In most cases it is not really practical to obtain a measurement of the overall waveguide loss that encompasses the full waveguide run from directional coupler to

feed horn. Moreover, any loss measurement involves both the ohmic and mismatch losses along the guide; in complex dual-polarization systems the mismatch losses can vary markedly with frequency (e.g., Figure 22). Consequently, waveguide loss measurements are mostly useful for performance monitoring purposes; measurements of effective antenna system gain (discussed in Sect. 2.2.5) adequately incorporate the losses for calibration purposes.

The ohmic losses vary only slowly with frequency and therefore one might expect measurements at only a single frequency to suffice. However, the mismatch reflections can be significant and can vary much more markedly with frequency (as in Figure 22); thus any loss measurements should actually cover a range of frequencies spanning the main part of the transmitter spectrum. This is especially important with Magnetron transmitters, where substantial frequency variations can arise.

As illustrated in Figure 22, a Network Analyzer can be conveniently employed to investigate waveguide loss measurements as a function of frequency. In that example the ohmic loss component of the measurements is no greater than about 1.5 dB; it could be less, because there is no assurance that the mismatch reflections completely cancel even at the minimum in the curve. However, the mismatch reflections can add another 1 dB or so (even more in some cases) to the measured values.

It should be stressed that differing frequency-dependent losses in the two channels contribute to a frequency dependent bias in Z_{dr} . (Table 12)

2.5.2 Directional Couplers

Radar systems typically include several strategically located directional couplers (Figure 23) that are used to safely connect built in or external measurement devices. Monitoring the calibration of these devices is important to collect reliable test measurements (though if the same forward port is used for transmitter power and antenna measurements as well as receiver calibration, the coupling factor cancels out of equations like (5) and the actual value is immaterial; Smith 1974). The same must be done for any attenuators that are employed to protect measuring devices such power sensors. Typically these items are sent to calibration facilities for certification “testing.”

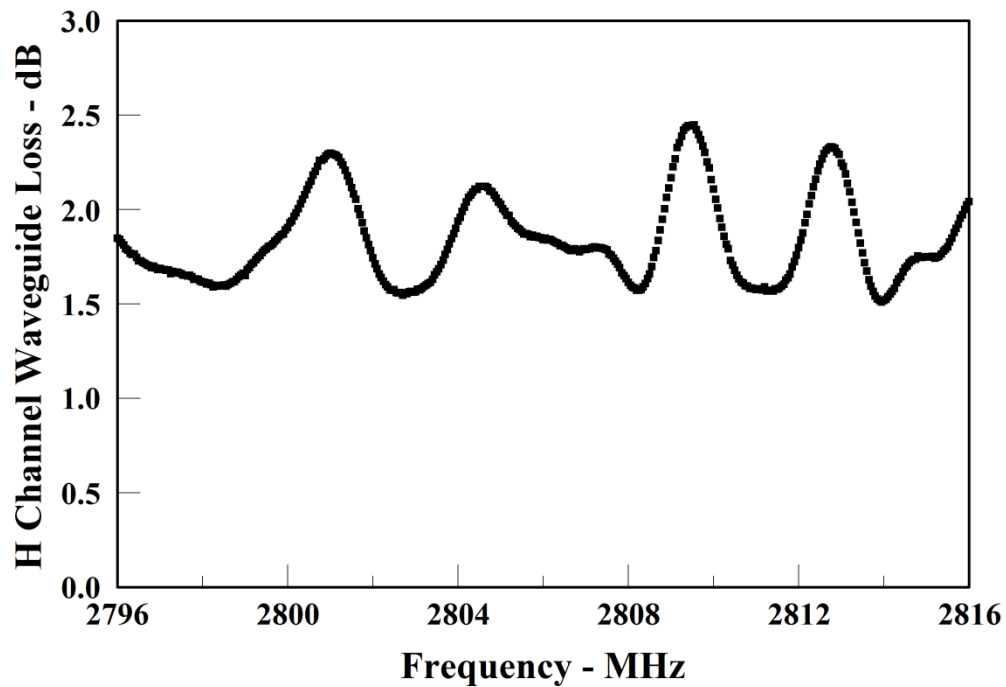


Figure 22: Example of data from a Network Analyzer sweep of the loss in dual-polarized radar.

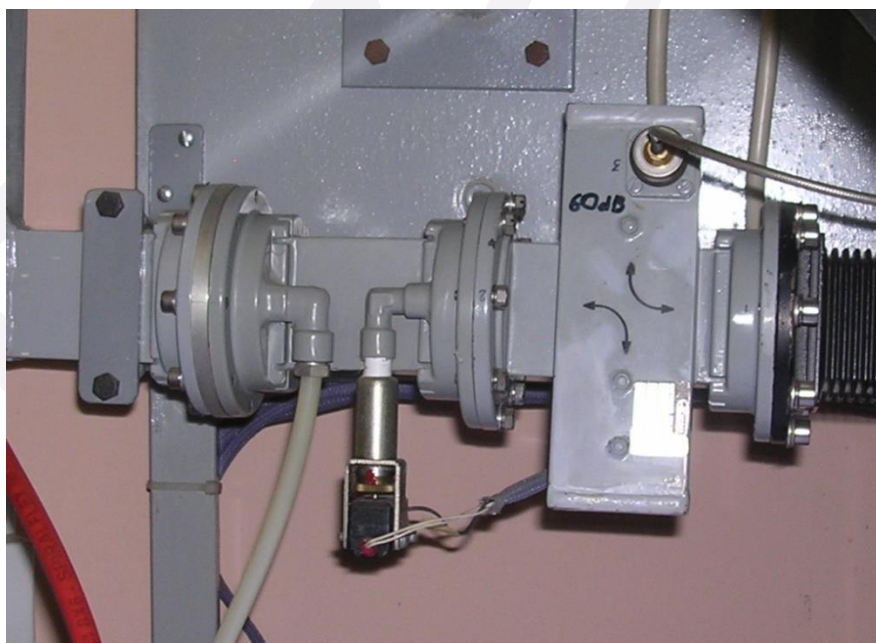


Figure 23: Calibrated 60-dB cross-guide directional coupler at the output of a klystron transmitter (Polar 55C, CNR; Italy). For most calibration purposes in-line bidirectional couplers are more useful.

3. END-TO-END CALIBRATION VALIDATION/VERIFICATION METHODOLOGIES

A weather radar system is composed of many components. The previous sections have shown that the tasks of characterizing each individual component or subsystem can be quite tedious. Fortunately, it is only necessary to conduct some of the tests on an occasional basis, or after some significant change to the system. However, for this reason it can also be convenient to use methodologies to evaluate and characterize the radar system as a whole. These end-to-end calibration tests involve the measurement of returns from scatterers with known signatures, such as standard reflectors or spheres with known radar cross sections, or determining some measurable and reproducible properties of returns from precipitation. Active external sources like the sun, although a valuable tool for some calibration and monitoring purposes, cannot be considered to provide an end-to-end calibration. In the following techniques based on point targets and properties of returns from the precipitation medium are described.

3.1 CALIBRATION USING POINT TARGETS

Metal spheres and corner reflector have known radar cross sections and are established standard targets for calibrating radars. In the following sections implementation of calibration experiments with trihedral reflectors and suspended or floating metallic spheres are described. Trihedral reflector calibration can be collected routinely with permanent setups, while specific calibration experiments must be planned using balloon-borne or tethered metallic spheres.

3.1.1 Trihedral reflectors

Trihedral reflectors are commonly used to routinely calibrate several categories of radar systems. Such a “corner reflector” is composed of three triangular conducting planes oriented so that each section is perpendicular to the others. Figure 24 shows a trihedral reflector with triangular faces that is commonly used for the calibration of radars. Figure 25 sketched a typical setup for corner reflector calibration. The reflectivity factor is computed from the received power using the equation (5) that is rewritten in logarithmic units as

$$Z_e(\text{dBz}) = \bar{P}_r(\text{dBm}) + C(\text{dB}) + 20\log_{10} r(\text{m}) \quad (20)$$

where C is the radar constant given by

$$C(\text{dB}) = 10\log_{10} \left\{ \frac{1}{\pi^5 |K_w|^2} \left(\frac{2}{c\tau} \right) \left[\frac{(4\pi^3)}{P_t G_0^2} \right] \left(\frac{8\ln 2}{\pi\theta_1\phi_{11}} \right) \lambda^2 10^{21} l_{tp} l_{rp} l_f l_d l_p \right\} \quad (21)$$

where l_{tp} , l_{rp} , are the transmit and receive path loss, respectively, l_f , l_p , l_d are the receiver finite bandwidth power loss, Probert-Jones integral correction, 2-way radome loss, respectively. The reflectivity factor can be obtained also by estimating it with reference to the received power from the trihedral corner reflector as

$$Z_e(\text{dBz}) = \bar{P}_r(\text{dBm}) + C_{cr}(\text{dB}) + 20\log_{10} r(\text{m}) \quad (22)$$

where \bar{P}_r is the digitized received power expressed in dBm and C_{cr} is the radar constant that in the case of a point target like the corner reflector is given by

$$C_{cr}(\text{dB}) = 10\log_{10} \left\{ \frac{1}{\pi^5 |K_w|^2} \left(\frac{2}{c\tau} \right) \left[\frac{\sigma_{cr}}{\hat{P}_{cr} r_{cr}^4} \right] \left(\frac{8\ln 2}{\pi\theta_1\phi_{11}} \right) \lambda^4 10^{18} l_f l_n l_p \right\} \quad (23)$$

\hat{P}_{cr} being the digitized received power from corner reflector, r_{cr}^4 the range from the corner reflector, and σ_{cr} is the radar cross section (RCS) of the corner reflector, and l_n is the near-field antenna gain loss for point target. The calibration constant C_{cr} circumvents the use of well calibrated measurements of the radar subsystems.

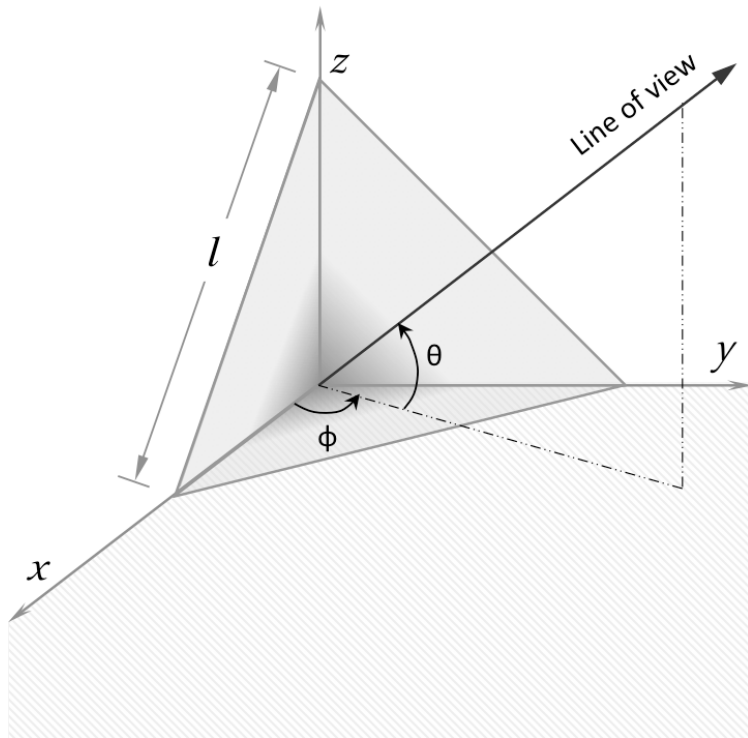


Figure 24: Geometry of a triangular trihedral corner reflector. The line of view is the direction of the bore sight of the antenna beam with respect to the corner reflector.

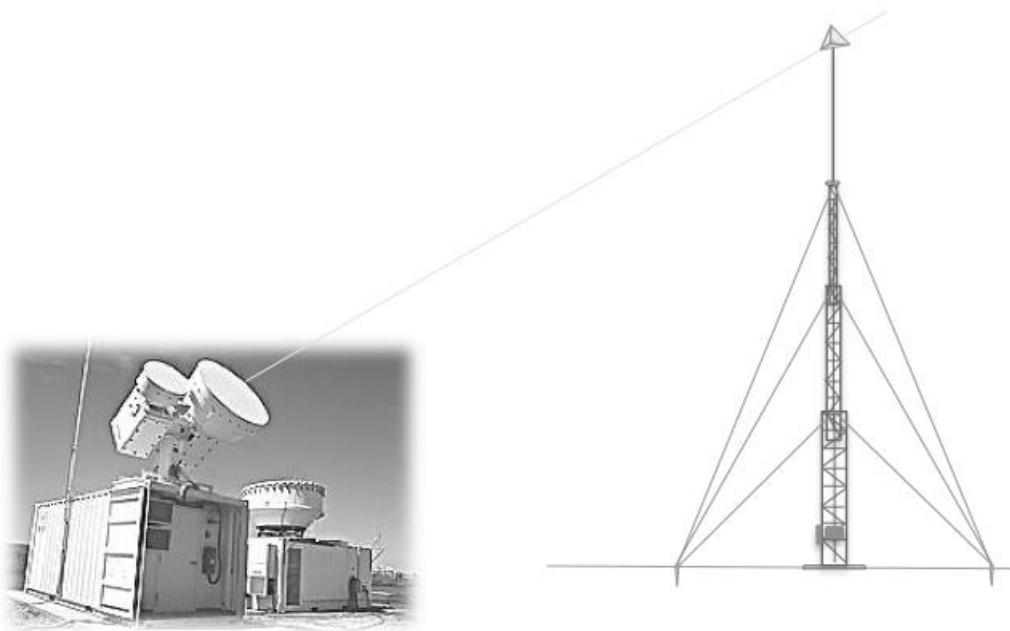


Figure 25 : Illustration of the setup for calibration with a triangular trihedral corner reflector.

The radar cross-section of a trihedral corner reflector is a function of the view angle of the radar beam. The maximum radar cross-section for the reflector with edge l is

$$\sigma_{cr} = \frac{\pi l^4}{3\lambda^2} \quad (24)$$

that occurs for a line of view corresponding to $\theta = 35.25^\circ$ and $\phi = 45^\circ$ which is the bore sight of the corner reflector. In practice, it is not always possible to have a line of view to provide the maximum radar cross-section. However, the trihedral reflector has a very wide field of view and the reduction in RCS is small. The RCS reduction is within ± 0.2 dB for angular offsets less than 5.0° .

The RCS of the trihedral is affected by the angular errors between the faces of the trihedral. The angular error in the manufacturing of the trihedral reflector is defined as the maximum offset angle from the faces being orthogonal (i.e. 90°) that with modern manufacturing methods the error in is well within 0.1 dB. The errors in RCS are negligible for centimeter wavelength radars when compared to millimeter wavelength radars.

3.1.1.1 Practical aspects

There are several factors that must be taken into account while performing end-to-end calibration with a trihedral corner reflector. Some of most significant factors are discussed in the following sections.

a) Transmitter and receiver configuration

The configuration of the transmit waveform and receiver is very important for performing calibration with a corner reflector. The key elements pertain to the closest observable range gate and receiver saturation. The received signal from a corner reflector can be very strong which will saturate the receiver in most systems. The observation setup must include mechanisms to negate receiver saturation. Receiver saturation can be eliminated by the addition of fixed attenuators in the front end of the receiver or incorporating a system to lower the transmitter peak power. The use of pulse compression waveforms in systems using klystrons, TWTs and solid-state transmitters is becoming more common for precipitation and cloud radars. The use of pulse compression waveforms inherently puts a limitation on the location of the corner reflector because of the blind range issues related to the use long pulses. The corner reflector must be located beyond the blind range, which may be much farther than the optimal region for locating the reflector. The need for the corner reflector to be located closer to the radar is described below.

b) Reflector location

The location of the reflector is very important to minimize the effect of ground clutter and multipath. The location of the corner reflector is primarily determined by the antenna beam width because the cross-range resolution degrades with range. The factors that must be taken into consideration for the location of the corner reflector are cross-range resolution, height of the reflector above ground and line of sight. The range to the reflector must be selected such that the beam size is small to avoid main-lobe clutter. If the beam is too wide, the main-lobe clutter will be too strong and shall introduce a bias in the calibration. Because the filtered echo from a point target is a smoothed version of the transmit pulse, it is also important with a pulsed transmitter and digital receiver to be sure the corner reflector is situated in the middle of the filter response in range. The height of the reflector is a function of the range and the requirements for the size of the tower becomes impractical if the reflector is too far. To avoid the need for a very large tower the reflector can be placed in the Fresnel region of the antenna without significantly affecting the observations. The line of sight is defined in terms of the waveforms ability to only observe the corner reflector which means there should be no structures (towers, trees, buildings, etc.) within the volume of the pulse while observing the reflector. Therefore, corner reflector calibration has its limitations while using pulse compression waveforms with long pulses.

c) Signal-to-clutter ratio

The corner reflector calibration assumes the received power corresponds to the radar-cross-section of the reflector. However, in practice the received signal is contaminated by clutter signal that biases the calibration constant depending on the signal-to-clutter ratio (SCR) and phase alignment of the signals.

Figure 26 shows the bounds on the bias introduced due to the presence of ground clutter signal. The bias is on the order of 0.25 dB or less when the SCR is greater than 30 dB. Observations with and without the reflector can be made to access the signal-to-clutter ratio. Since both ground clutter and returns from the reflector have zero Doppler velocity, traditional clutter filters cannot be applied to suppress ground clutter. Another approach is to have the reflector on a moving platform to introduce Doppler velocity on the received signal. Figure 26 shows the observations of the corner reflector region with and without the reflector on the tower. The observations are made with Ka-band Scanning ARM Cloud Radar (Ka-SACR), which operates with a 0.33 degree beam width. With a reflector size chosen to have adequate RCS for Ka-band it can be observed in Figure 27 that SCR is sufficiently high to keep the bias within ± 0.25 dB.

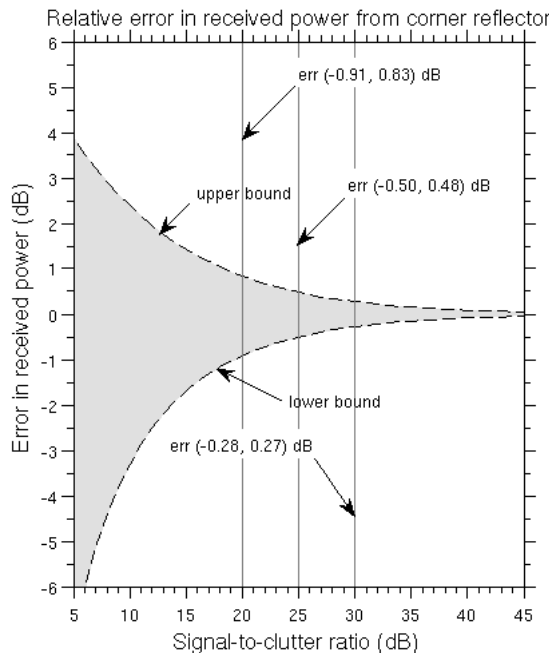


Figure 26 : Bounds on the bias in received signal power from corner reflector as a function of signal-to-clutter ratio.

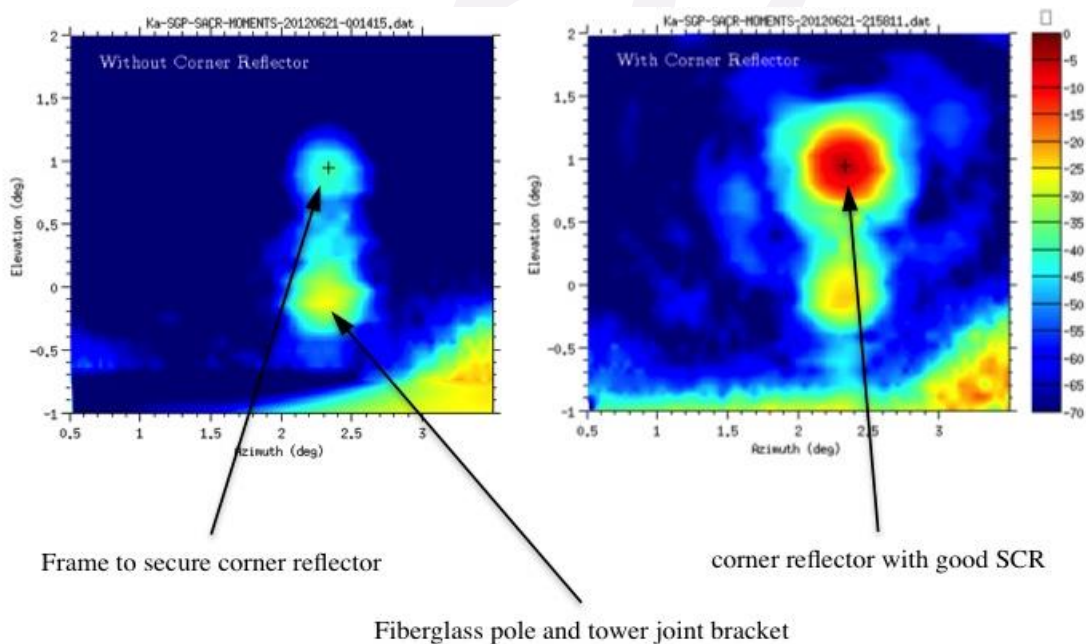


Figure 27 : Received power (relative to corner reflector) of a 55 feet tower with and without a trihedral corner reflector. The observations were made with Ka-band Scanning ARM Cloud Radar (Ka-SACR).

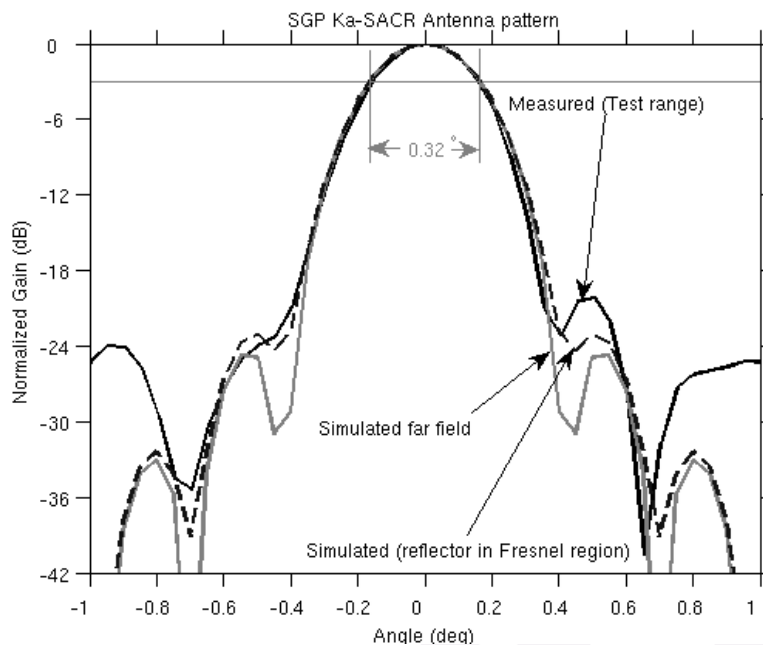


Figure 28 : The antenna pattern of Ka-SACR from test range along with the simulated far field and Fresnel region antenna pattern.

d) Antenna pattern

In general, the data used in applications and retrievals are observations in the antenna far field. The corner reflector is located in the Fresnel region to mitigate some of the practical issues with beam size and tower heights. The observations of the corner reflector are made in the Fresnel region of the antenna pattern where antenna beam shape is already well formed, well beyond the near field of the antenna. The gain of the antenna is lower in the Fresnel region when compared to the far-field gain. The antenna pattern in the far field and Fresnel region for a circular aperture is simulated for Ka-SACR. The simulated patterns are shown in Figure 28 along with the pattern measured in a test range. The Fresnel region pattern is simulated for a corner reflector located at about 460 m from the radar. It can be observed that the beam shape is well formed and closely matches the test range measurements in the main lobe of the antenna. The patterns shown in Figure 28 are normalized to the gain. The gain of the antenna in the Fresnel region is computed numerically to obtain the correction for the received power. The correction is small as the reflector locations approach the far field of the antenna.

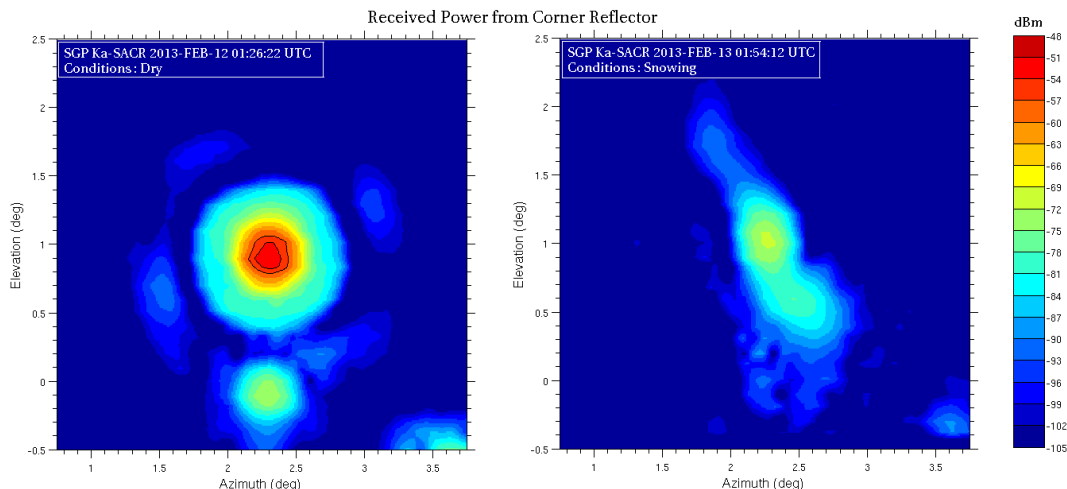


Figure 29 : Comparison of corner reflector observations without (left) and with (right) precipitation.

e) Environmental conditions

The environmental conditions in which the corner reflector observations are made have a significant impact on the usefulness of the data for calibration. The environmental conditions consist of three main factors. One, the atmospheric state of the path between the radar and the reflector has a significant effect on the received power. At higher attenuating frequencies the presence of precipitation biases any calibrations done with a corner reflector. Two, the state of the surfaces on the corner reflector has an impact on the received power. The presence of layers of water or icing on the reflector surfaces changes the RCS and introduces larger uncertainties. Three, the state of the radome makes significant contribution to errors in calibration. Under condition of rain over radome, wet radome or icing on radome the received power from corner reflector cannot be used for calibration. Observations of corner reflector with data collected on a clear day are compared to data collected in a precipitating event in Figure 29. The precipitating event most likely resulted in some form of icing on the radome due to wet snow and ice. The adverse effects of the environmental conditions are clear in Figure 29. The received signal is attenuated by more than 20 dB compared to the data collected on a clear day. Corner reflector data should be used for calibration if and only if the data is collected under clear air conditions.

3.1.2 Calibration sphere experiments

Spherical conducting reflectors have well-known radar cross sections and excellent polarization isolation to linearly polarized waves and can be used to establish absolute calibration and balance of H and V channels in dual-polarization systems.

A metallic sphere is a good point target because its RCS can be precisely calculated and is the same RCS from any viewing angle. Figure 31 reports the well-known relationship of the RCS of the sphere with the radar wavelength and the sphere's physical diameter. The radar equation for a metal sphere in the bore-sight of the antenna, in the center of the along-range filter response, and in the far-field can be written as

$$P_{ref(ms)} = \frac{\lambda^2 P_t G_0^2 \sigma_{ms}}{(4\pi)^3 l_{wg}^2 r_{ms}^4} \quad (25)$$

where the subscript 'ms' represents the metal sphere and l_{wg} is the waveguide and radome loss expressed as a numerical factor >1 . Rearranging the terms of this radar equation gives the antenna gain as

$$G = \frac{G_0}{l_{wg}} = \sqrt{\frac{(4\pi)^3 r_{ms}^4 P_{ref(ms)}}{\lambda^2 P_t \sigma_{ms}}} \quad (26)$$

where G plays the role of the effective antenna system gain with waveguide and radome loss factored in.

Calibration experiments can be implemented using either tethered or floating spheres. However, with a balloon-borne object it is difficult to get the target (especially a moving one) centered within both the beam width and the along-range receiver filter response. Oversampling the echo can assist with the latter, but considerable effort may be involved in acquiring the proper data.

The typical implementation of the experiment makes use of a metallic sphere (aluminum, or just Styrofoam coated with a metallic foil) suspended by a tethered balloon. A 600 gram helium filled balloon is sufficient to loft a 12 inch diameter Styrofoam sphere wrapped with aluminum foil. The main disadvantages of this method lie in the uncertainty in the actual position of the sphere. The height of the sphere should be enough to avoid interferences from ground targets, which are often a problem with tethered-sphere calibrations. A different implementation is the use of a free-flying sphere.

Figure 30 shows the preparation of 12-inch sphere and the balloon for a calibration experiment based on a free-flying sphere. The balloon is released and tracked optically at first, with a theodolite, to a distance beyond some 5 kilometers downwind of the radar.



Figure 30: Preparation of a free-flying sphere for a calibration experiment at CSU CHILL facility supervised by one of the authors (VC).

Its position is relayed to the radar operator, who then sets a tight sector scan to cover the position of the sphere. The antenna gain is calculated with (26) using the maximum received power of each traverse across the sphere. A histogram can be made from these gain calculations; Figure 32 reports the results of such a calibration experiment as performed at the CSU-CHILL facility.

Further outcomes can be obtained from data collected during a sphere calibration experiment. In addition to helping to obtain data with the sphere in the center of the along-range filter response, oversampling of the echo in range can allow reconstruction of the transmitted pulse envelope. Figure 33 shows the good agreement in results obtained with 333 ns oversampling of the echo of a 1.5 μ s pulse from a sphere.

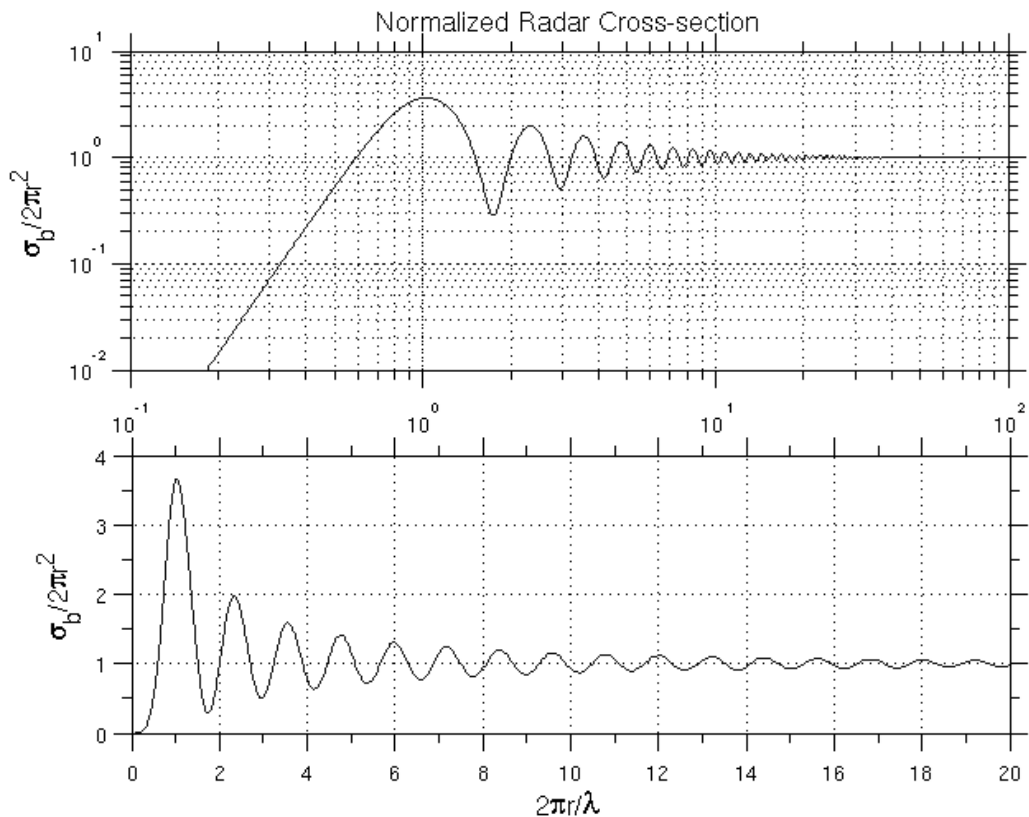


Figure 31: Normalized radar cross section of a metallic sphere as a function of the normalized diameter.

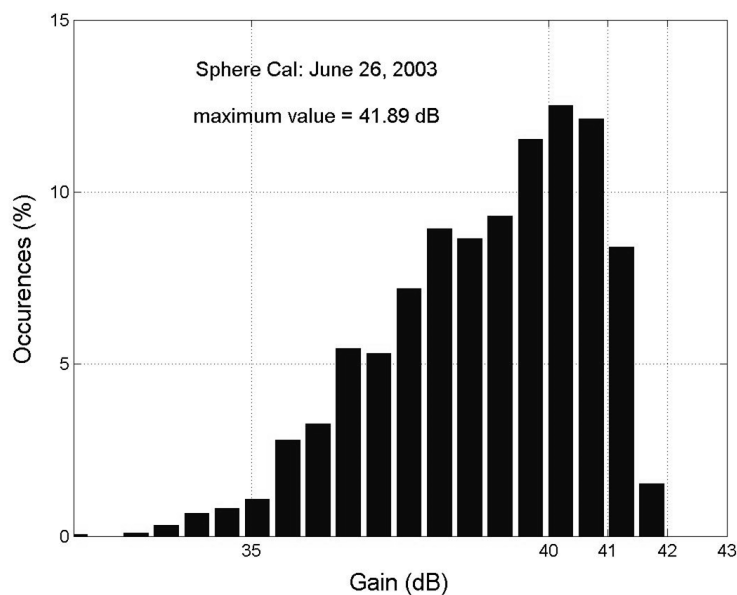


Figure 32: Estimation of antenna gain using data from a sphere calibration experiment.

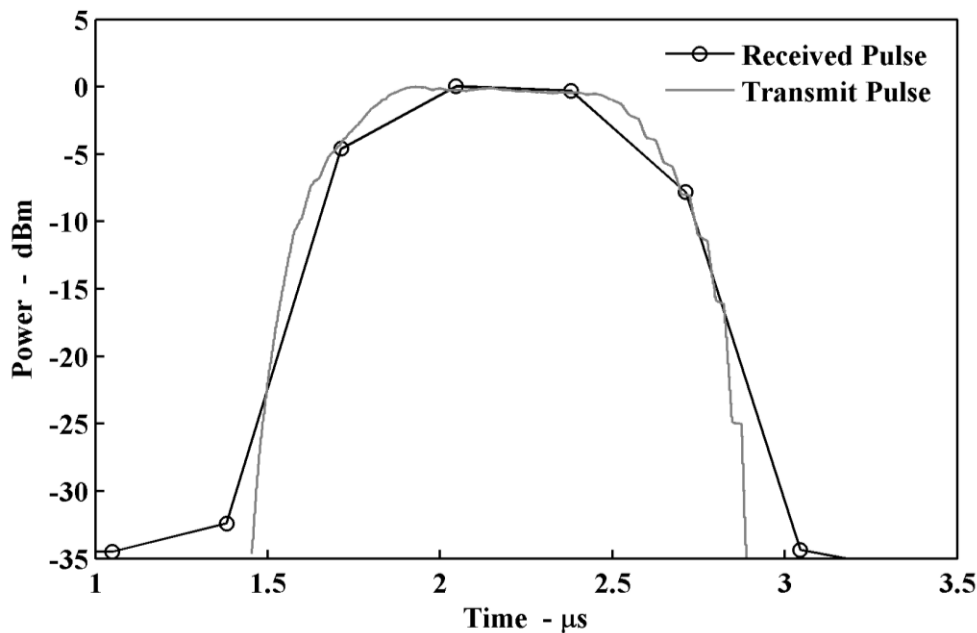


Figure 33: Comparisons of the directly-measured transmit pulse and the estimated pulse waveform from the sphere return (*CSU-CHILL, experiment of September 23, 2011*).

3.2 USE OF RETURNS FROM PERMANENT SCATTERERS

The use of cluttered echoes generated from permanent and spatially localized structures, such as towers or other buildings, collected at low elevation angles to monitor the stability of calibration in time as been suggested by Rinehart (1978) and adopted at the NASA KPol S-band radar at Kwajalein Atoll (Silberstein et al. 2008) to check the day-to-day stability of radar calibration. The basic idea is that stability of clutter echoes reveals stability of radar calibration, provided that no changes in structures are made, radar elevation angle is constant in time, the contribution of precipitation does not dominate the contribution from clutter, and, finally, effects of anomalous propagation can be neglected. The method starts from identification of cluttered bins of from scan collected in dry conditions using a low elevation

angle (0.4° is used at K-Pol). On a daily basis, cumulative distribution functions (PDF) of equivalent reflectivities (dBz) recorded at identified bins are built. Of course, reflectivity data without clutter filtering must be used. Evaluation of 95th percentile of daily CDFs, subtracted from a baseline value provides the RCA (relative calibration adjustment) in dB. The RCA is evaluated daily regardless of presence of precipitation, when the equivalent reflectivity is the sum of clutter and rain reflectivity, since it has been shown that the presence of precipitation does not alter the 95th percentile of CDF used to evaluate the RCA. At very short ranges (shorter than 1 km) the stability of cluttered bins has been evaluated to be better than 0.07 dB, while daily fluctuation of RCA increases up to 0.21 dB within 10 km range. The use of this technique has allowed to correlate sudden changes in RCA to damage or engineering events, and to shift in elevation pointing.

3.3 USE OF RETURNS FROM PRECIPITATION

Weather radars are designed to sample distributed volume filled targets like precipitation. On the contrary, the spherical or corner reflectors considered in the previous section are point targets and not completely representative of the targets of main interest with weather radars. Echoes from precipitation have several properties that can reveal calibration biases or highlight other aspects characterizing the performance of the radar system. These methods have the advantage of being performable during routine operations when suitable precipitation targets are available.

3.3.1 Differential reflectivity calibration

A commonly suggested option for calibrating Z_{dr} is the use of differential reflectivity measurements collected at vertical incidence (Seliga et al. 1979). This method relies upon the assumption that, due to the symmetry of the particles when viewed from below, the average Z_{dr} in precipitation should be zero at vertical incidence. In fact, cloud and precipitation particles have no preferential orientation in a horizontal plane: ice particles are usually randomly oriented and rain drops present, on average, a circular shape. Consequently, any observed departures from zero Z_{dr} can be ascribed to a bias of the radar system due to some differential response between the two channels, and a suitable offset correction applied to subsequent Z_{dr} data should be applied.

Usually vertically-pointing differential reflectivity calibration measurements are performed with a rotating antenna that implies that the polarization basis is rotated. In fact, rotating the antenna should reduce the influence of any azimuth dependency of Z_{dr} , which may be caused by the possible presence of aligned hydrometeors (e.g., due to strong wind shear or electric fields), antenna pattern sidelobes interacting with ground clutter (Gorgucci et al. 1999), or back lobes that interact with the precipitation (Hubbert et al. 2003). Measurements in the melting layer or in layers with heterogeneous scatterers or strong gradients should be avoided because Z_{dr} data would exhibit larger measurement errors compared to more homogenous layers. Many operational radars do not operate at vertical incidence due to mechanical constraints or choices in the scanning strategies. If a weather radar has no mechanical constraints, including an occasional scan along the vertical incidence direction in the observational scanning strategy is highly recommended both to verify the calibration of Z_{dr} and to add a high-vertical resolution description of the column of the above the radar. In case of limitations due to mechanical constraint, other techniques to calibrate Z_{dr} use the collection of data at near-horizontal elevation in drizzle or light rain, thought to be mainly composed of very small and spherical droplets determining a differential reflectivity around 0 dB (Seliga et al. 1979; Smyth and Illingworth 1998). Observations of light drizzle that deviate from zero Z_{dr} can thus be considered to indicate a Z_{dr} bias. However, it is sometimes difficult to clearly identify drizzle echoes, especially in low SNR. Otherwise, measurements exploiting the dependency on elevation of Z_{dr} measurements in stratiform rain and dry aggregated snow can be used to calibrate Z_{dr} (Bechini et al. 2008) by comparing measured Z_{dr} profiles in elevation with the corresponding theoretical profile. Several hours of uniform precipitation are needed to achieve accuracy within 0.1 dB.

3.3.2 Absolute reflectivity calibration

An absolute calibration of weather radar can be established from measurements of Z_h , Z_{dr} and K_{dp} in rain using the “self-consistency” among these measurements (Gorgucci et al. 1992, Goddard et al. 1994, Scarchilli et al. 1996). The “self-consistency” leads to a relation of the form

$$K_{dp} = aZ_h^b Z_{dr}^c \quad (27)$$

where coefficients a , b , and c depend, among other things, on the assumed shape-size relation of raindrops. Supposing Z_{dr} unbiased and Z_h affected by a bias B_h , integrating the previous expression along a radial path r_1-r_2 , B_h can be obtained from

$$B_h(\text{dB}) = \frac{10}{b} \log_{10} [\Phi_{dp}(r_2) - \Phi_{dp}(r_1)] - \frac{20}{b} \log_{10} \int_{r_1}^{r_2} a_3 Z_h(r)^b Z_{dr}(r)^c dr. \quad (28)$$

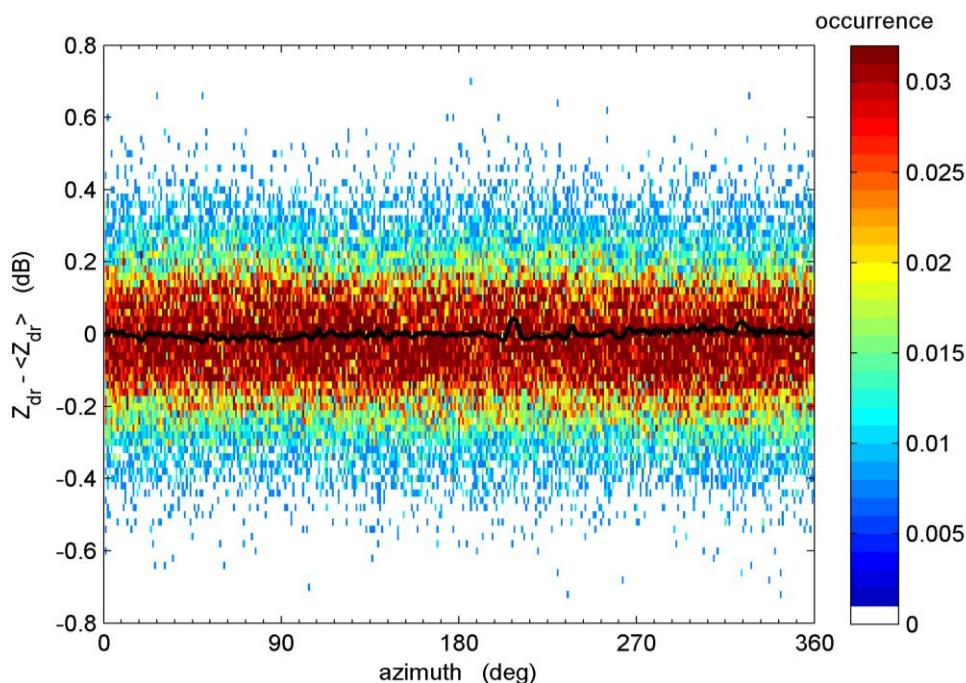


Figure 34: Example of the scatter of vertically-pointing Z_{dr} measurements as a function of azimuth during antenna rotation (Polar 55C measurements).

Operational implementation of the method requires some care. First, the self-consistency properties are valid only in rain. Therefore rain profiles contaminated by ground clutter, melting layer or ice particles should be discarded and not considered in the method. Second, the length of paths should be chosen to minimize the measurement error associated to the computation of the Φ_{dp} difference. When this method is used with attenuating frequencies, such as those at C-, X-band or higher frequencies, the path attenuation, and, eventually, the attenuation induced by the wet radome must be also corrected. Coefficients of the self-consistency relations depends on the radar wavelength, temperature and assumptions on drop shape relations.

In general working with such data is ONLY a monitoring tool, and not a replacement for engineering calibration procedures. Because of the possibility of wide fluctuations in data, any observed calibration difference using precipitation data should be used as a clue suggesting very thorough engineering tests. Otherwise, it will create a situation of “circular argument”.

3.3.3 Other polarimetric measurements

In addition to the properties suggested in the previous section, other properties of dual polarization measurements can be used as diagnostic tools. Information about performance that can be updated on a daily or on a per event basis helps to detect issues in the system. Most of these properties are relative to returns from rain.

Some of them are summarized in the following.

a) *Noise level estimation.*

To obtain an on-going measure of the receiver sensitivity, the noise from areas where precipitation returns are absent (e.g. far ranges at high elevations) can be used to verify the actual noise level and its constancy in time.

b) *Azimuth dependent bias.*

In widespread light rain (20-40 dBZ), differential reflectivity should be essentially constant across all azimuths.

c) *Daily-averaged ρ_{hv} value in rain.*

In homogenous precipitation a value close to 0.99 is expected.

d) *Azimuth-dependent $\Phi_{dp}(0)$.*

The initial differential phase should be constant and independent of azimuth. Variation from the average could reveal radome or waveguide component degradation.

e) *LDR limit.*

Minimum detectable LDR in systems with this capability provides an overall estimation of the cross-polarization isolation of the system.

4. BUILT IN MONITORING TOOLS AND “AUTOMATIC CALIBRATION”

Some of the detailed processes in the radar calibration operations discussed above require the involvement of expert personnel. However, given the importance of calibration, weather radars can be equipped with some proper self-calibration “sub systems”, to allow continuous monitoring of elements contributing to the variations in the calibration of the system. The concept to set up a built-in calibration system can be understood by looking at equation (3) rewritten by explicitly grouping P_t and P_r in a ratio to obtain

$$Z_e = \frac{1}{\pi^5 |K_w|^2} \left(\frac{2}{c\tau} \right) \left[\frac{(4\pi)^3}{G^2} \right] \left(\frac{8\ln 2}{\pi\theta_1\varphi_1} \right) \lambda^2 r^2 \left(\frac{P_r}{P_t} \right). \quad (29)$$

Although mathematically equivalent to (3), this formulation highlights that reflectivity can in principle be determined by the measurements of a power ratio, rather than by two independent measurements of P_t and P_r . In fact, the mean power at the receiver in (5) historically has been by expressing related to the equivalent reflectivity factor and the radial distance by a factor C , i.e. the radar constant that includes as in P_r (e.g., Battan 1958):

$$P_r = C \frac{Z_e}{r^2}. \quad (30)$$

In (29) the only thing we need to monitor on a continuous basis is the ratio P_r/P_t , and this ratio can be measured by passing both signals through the same digital receiver. The main issue is that the losses in the measurement paths of transmit power and receive power are different. Therefore, elaborate strategies to do “proper book keeping” have to be devised. The good news is these “loss terms” are constant.

4.1 CSU-CHILL IMPLEMENTATION

The schemes illustrated in this section show how to collect, in a single sweep, the ratio P_r/P_t by taking into account the different paths needed to measure both quantities. Moreover, given that today's receivers can only process input signals of power typically up to like -25 dBm (see Figure 21 for a typical receiver transfer function), proper attenuators must be inserted to obtain transmit power measurements with the receiver. Basically, switches in the microwave circuits permit automatic self-calibration in this manner using the digital receiver and signal processor. As a first hypothesis passive elements, like waveguides and cables, are assumed to not change significantly between scheduled maintenance operations. The critical elements that may vary are the active components. During operations, system control can command periodic calibration procedures that characterize the active components to resolve any such unknowns: a calibration database can be used to detect anomalous calibrations and flag them for further investigation. Figure 35 shows a schematic diagram (CSU-CHILL is taken as a reference example) of a radar implementing such circuits. All measurements are made with respect to the radar calibration plane, which is set in this case at the forward port of the 35 dB bidirectional coupler.

In the standard receive configuration, (Figure 36) a high-speed switch sets to receive position after a fixed delay $\Delta\tau$ (3 μs for CSU-CHILL) from the transmit pulse. Returns pass through the circulator, and get into the usual receiving channel, passing through the low noise amplifier (LNA) and the down-converter to the Digital receiver. If the antenna receives a power P_{RX} , the digital receiver has IF input $S_{RX} = P_{RX} + G_{LNA} + G_{DC}$, where G_{LNA} and G_{DC} are the gain of the low noise amplifier and down converter, respectively. Both G_{LNA} and G_{DC} need to be determined, or they can be grouped into the composite front-end conversion gain G_c as in Sect. 2.3.1.2.

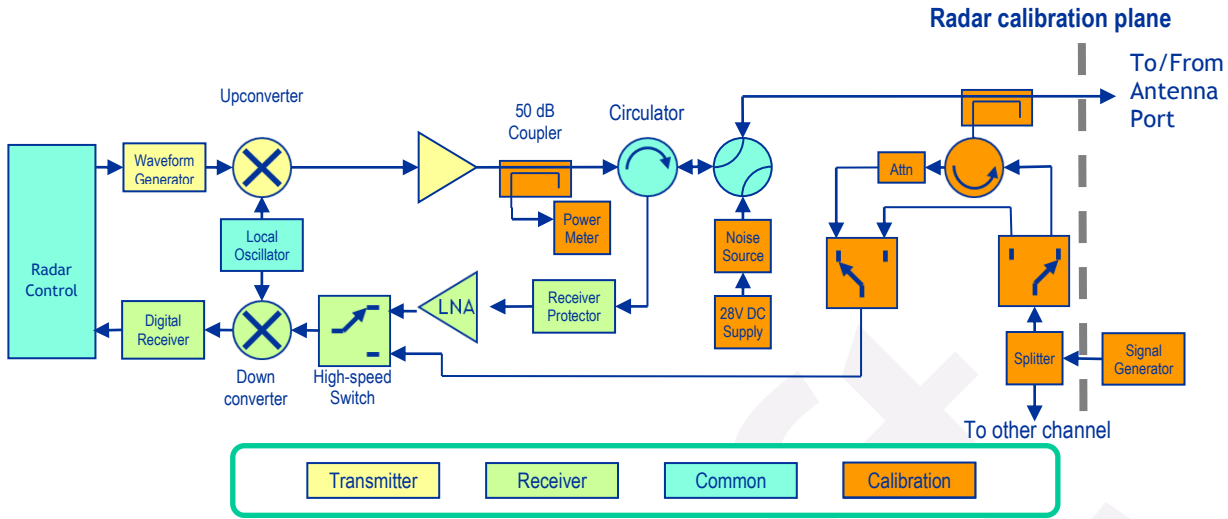


Figure 35: CSU-CHILL radar configuration. Different colors are used to distinguish radar subsystems. Orange boxes identify calibration subsystem. Only one polarization channel is shown.

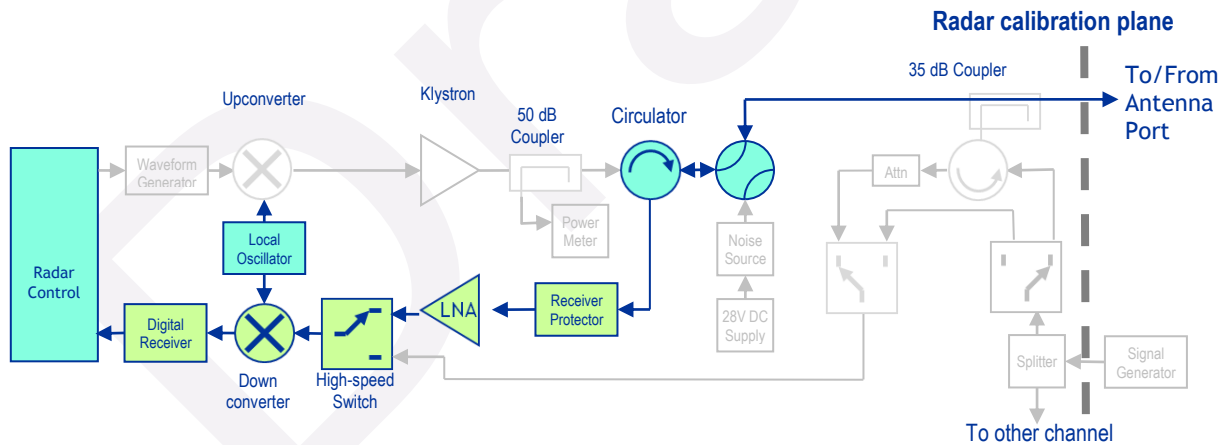


Figure 36: Configuration of Figure 35 in the normal receive mode.

The configuration of Figure 35 can be set up to measure the transmit pulse as shown in Figure 37. Within the transmit pulse and the subsequent $\Delta\tau$ delay, the high-speed switch is set in the *cal* position to measure the transmit power using the digital receiver and the same RF chain active components as the received signal, except for the LNA and receiver protector. Compared to a different configuration with a switch in front of the LNA, this configuration

avoids the associated increase in the noise figure. With this configuration, the digital receiver measures the power $S_{TX} = P_{TX} + G_{DC}$ (the attenuator is suppressed being a known value).

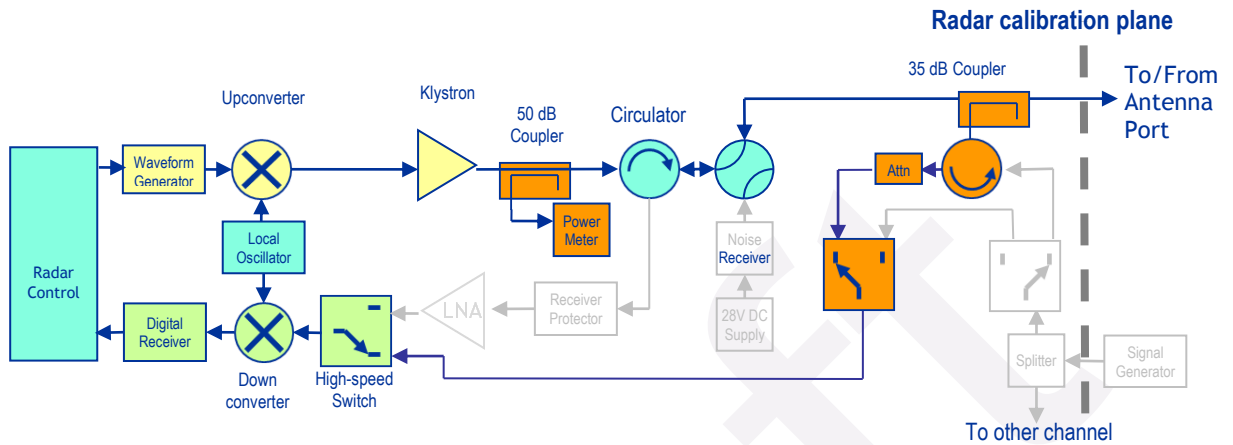


Figure 37: Configuration of Figure 35 for pulse transmission measurements.

To determine these unknowns in the configuration of Figure 35 a known signal power, P_{TEST} , is injected into the radar reference plane from an RF signal generator as in Figure 38. This measurement is done during data collection by pulsing the signal generator at a fixed range offset. The digital receiver measures $S_{TEST} = P_{TEST} + (G_{LNA} + G_{DC})$. Since P_{TEST} is known, $(G_{LNA} + G_{DC})$ is obtained directly from S_{TEST} .

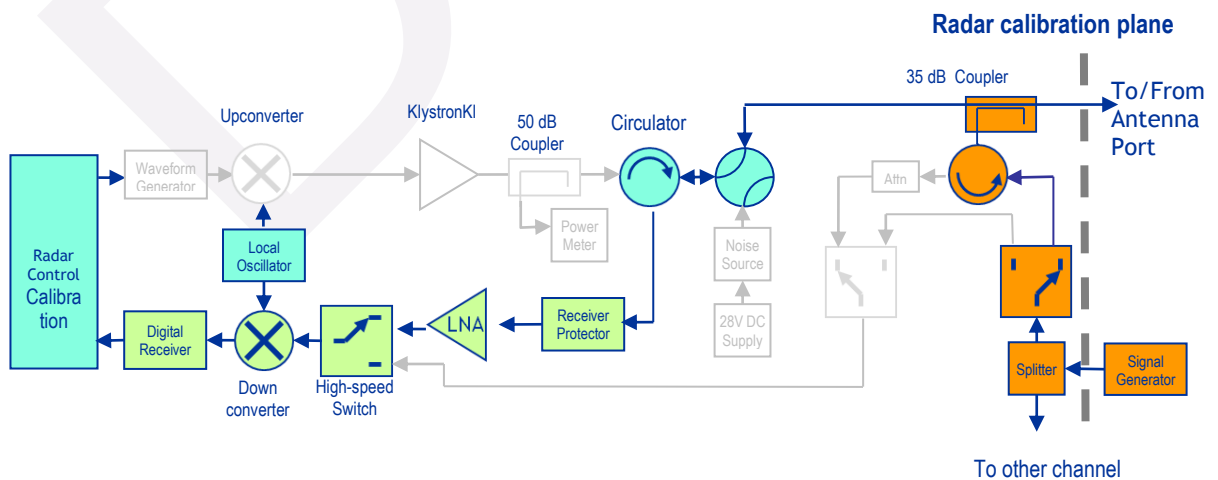


Figure 38: Configuration of Figure 35 for LNA and downconverter gain calibration mode

To resolve the separate estimation of the LNA and downconverter gains, the configuration in Figure 39 is adopted. A signal of known power, P_{TEST} , is injected into the calibrator from the RF signal generator. The digital receiver now measures $S'_{TEST} = P_{TEST} + L_{coupler} + G_{DC}$, where $L_{coupler}$ is the loss of the coupler. Since $L_{coupler}$ is known, G_{DC} can be computed and G_{LNA} can be determined from the $(G_{LNA} + G_{DC})$ previously estimated. A further element that can be estimated using this configuration is the receiver noise figure. To measure the noise figure (NF), a Noise Source of known Excess Noise Ratio (ENR) is used. Noise figure calibration using the Y-factor method (Hewlett-Packard, 1983) can be obtained as follows, using the radar in the configuration shown in Figure 39. At step 1, noise from a source of known ENR is injected and the digital receiver measures S_{HOT} . At step 2, the 28-Volt supply is turned off and the power from a “cold” source, S_{COLD} , is measured by the digital receiver. Finally

$$NF = ENR - 10 \log_{10} \left[10^{S_{HOT} - S_{COLD} / 10} - 1 \right] \quad (\text{dB}) \quad (31)$$

allows one to determine the NF in dB.

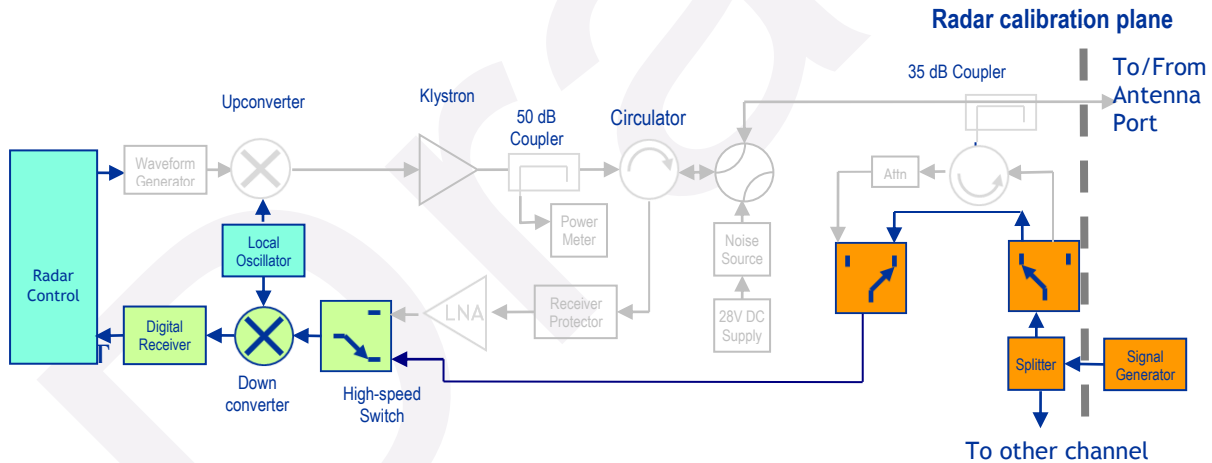


Figure 39: Configuration of Figure 35 for downconverter gain calibration mode

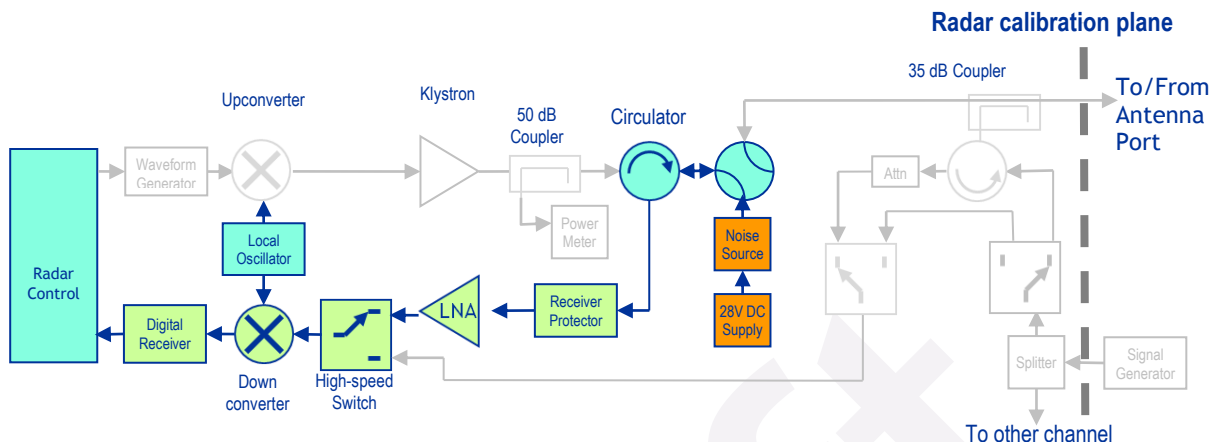


Figure 40: Configuration of Figure 35 to determine the receiver's noise figure .

4.2 IMPLEMENTATION FOR SYSTEMS WITH MAGNETRON TRANSMITTER

With systems using magnetron transmitter, the automated calibration process must take into account possible shift of operating frequency. An on-board calibration signal source allows automatic measurement of the gain of the receiving chain. Passing a sample of the transmitted pulse through the calibrated receiving chain allows keeping track of the changes in transmitted power decoupling them from receiver gain changes over time and/or frequency. If the transmitter is expected to operate in a broad frequency band, a broad-band signal source and automatic frequency control (AFC) style frequency measurement tool can be employed to measure receiver gain at the frequencies of interest and select the appropriate values during operation of the radar. Again, having an on-board calibration source allows repeating/automating the process as deemed necessary to track changes in time. To calibrate the receiver, a calibrated signal source the joint receiver and data acquisition system (DAQ) gain can be characterized at the transmitter frequency(ies) of operation as

$$G(f, t) = P_{SRC}^{DAQ}(f, t) - P_{SRC}(f) + G_{DX}(f) \quad (32)$$

where $G_{DX}(f)$ represents the gain characterization of the duplexer (it one-time measurement that can be done with a Network Analyzer). This equation allows referencing gain to the

antenna ports where the radar equation is applied. Concerning transmitter measurements, an initial measurement of the transmitted pulse power at the antenna port(s) is paired with the corresponding pulse sample measurement at the data acquisition output imposing

$$P_{TX}^{ANT}(f_0, t_0) \equiv P_{TX}^{DAQ}(f_0, t_0) \quad (33)$$

Transmitted power measured at the data acquisition system output is corrected for receiver gain variations to establish changes in transmitted power

$$\Delta P_{TX}^{DAQ}(f, t) = P_{TX}^{DAQ}(f_0, t_0) - P_{TX}^{DAQ}(f, t) - [G_{RX\ DAQ}(f_0, t_0) - G_{RX\ DAQ}(f, t)] \quad (34)$$

The transmitter-receiver calibration values can be finally incorporated into the radar equation as:

$$Z_e = \frac{2}{cT_0} \frac{c^2(4\pi)^3}{f^2 G_0^2} \frac{8 \ln 2}{\pi \theta^2} \frac{r^2}{\pi^5 |k_w|^2} \frac{P_{RX}^{ANT}}{P_{TX}^{ANT}} \quad (35)$$

where the knowledge of the transmitted frequency is used to select the appropriate calibration values.

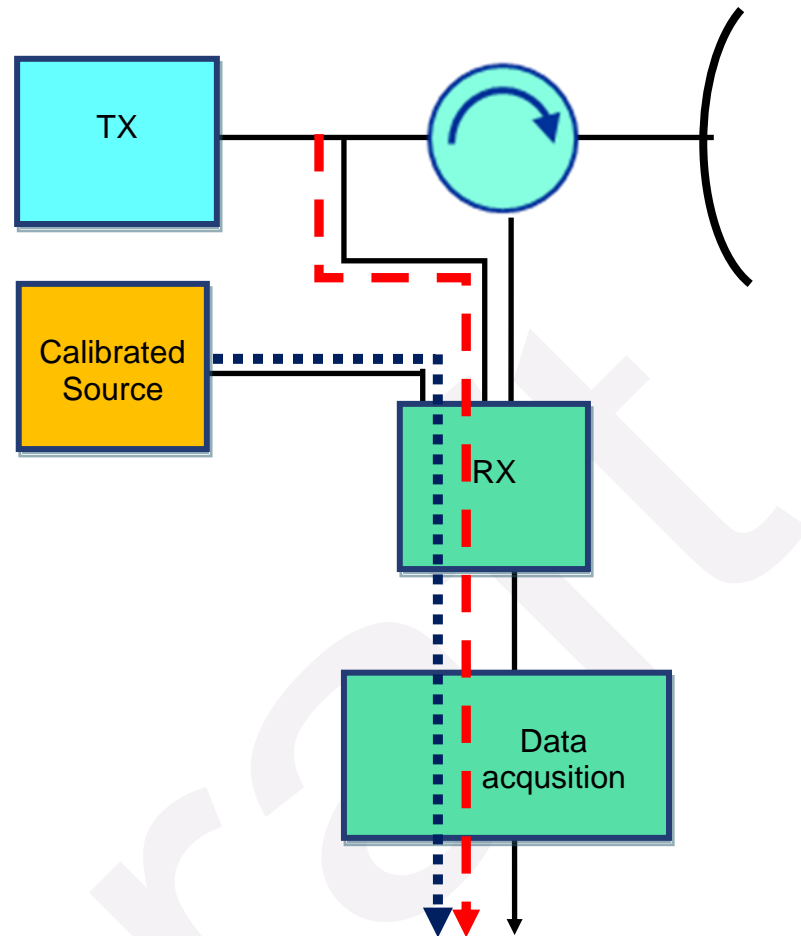


Figure 41: Configuration of calibration paths of a radar with magnetron transmitter using a calibrated source. Receiver and transmitter calibration paths are shown in dash and dot lines, respectively.

5. CALIBRATION PROTOCOL

5.1 INVENTORY OF TECHNIQUES AND EQUIPMENT

Previous sections have shown that calibrating a weather radar requires a combination of different techniques, corresponding to each subsystem. Several instruments are required. Moreover, the proposed techniques need to be implemented on a regular basis, with a calibration discipline. Instruments necessary to implement them are listed in Table 5.1.

5.2 RECOMMENDED PRACTICE

Table 5.2 provides an overview of the techniques introduced so far with a short description and the recommended frequency of implementation. Summarizing, a minimum set procedures to be implemented is that described below.

- 1) Receiver calibration –once every scan
- 2) Transmit power monitoring –continuous
- 3) Sphere calibration –once a year
- 4) Z_{dr} calibration - every volume scan with the modern operational calibration system. Vertical looking –Target of opportunity; Solar measurements –can be done routinely every day.
- 5) Solar calibration monitoring and ground target monitoring can be done very regularly and frequently.

6) Overall once a year calibration campaign is recommended

Finally, calibration requires discipline, to avoid rearrangement of equipment/connections. This is perhaps the most complicated of all the calibration procedures discussed, since some of them require stoppage of regular data collection. This should be scheduled based on weather forecasts to avoid loss of critical data.

Draft

Table 5.1 – Summary of calibration equipment

Instrument	Description	To be used for	Comments
Attenuator	e.g. Sect 2.1	protect whatever test instrument	
BITE	Sect. 4	Routine monitoring	
Clinometer or gunner's quadrant	Sect. 2.2.1.1	Servo/antenna data system verification	Expert operator required
Crystal Detector	Sect. 2.1.2	Signal envelope measurements	Used with oscilloscope, matched-impedance cable and termination
Dummy load	Secs. 2.2.8.2 and 2.3.3	analysis of reflected signals, Noise figure measurements,	
Metallic sphere	Sect. 3.1.2	End-to-end calibration	
Network Analyzer	Secs. 2.2.8, 2.5.1	WSWR; waveguide loss	
Oscilloscope	Secs. 2.1.2 and 2.2.8.2	Shape of transmit pulses/reflected signals	
Power meter	Sect. 2.1, 2.2	Transmit power; antenna measurements	Average power measurements preferred
Pyramidal standard gain horn	Sect. 2	Antenna pattern and antenna gain measurements	
Signal generator	Secs. 2.2.2 and 2.3.1	Antenna calibration; Receiver calibration	
Solar Scan Utility	Sect. 2.2.1	Antenna positioning; Antenna radiation pattern	Implemented at signal processor level
Spectrum analyzer	Sect. 2.1.2	Transmit spectrum	
Trihedral corner reflector	Sect. 3.1.1	End-to-end calibration	Permanent set up possible

Table 5.2 – Summary of calibration practices

Parameter	How to Conduct	Recommended Frequency
Transmit frequency	Counter, frequency meter or spectrum analyzer	Daily
Pulse shape	Crystal detector and oscilloscope	Weekly
Transmit spectrum	Spectrum analyzer	Once a year, unless transmit signal changes
Transmit power	Power meter	Daily
Transmit power stability	BITE	Continuous
Receiver calibration	Signal generator	Weekly
Receiver calibration stability	BITE	Once every scan
Antenna orientation	SSU	Quarterly
Antenna return loss (VSWR)	Power meter	Weekly
Corner reflector	Fixed set up as in sect. 3.1.1	Continuous when possible
Sphere calibration	Tethered or free floating sphere, depending on logistics	Once a year
Z_{dr} calibration, Vertical looking y	Sect. 3.1.2	when suitable precipitation occurs overhead
Z_{dr} calibration, Solar measurements	Solar measurements	Can be done routinely every day.
Solar calibration monitoring		Can be done very regularly and frequently
Ground target monitoring	Routine or special scans	Can be done every scan if target is routinely visible
Calibration campaign	As described in Sect. 2, including standard gain horn measurements	Once a year

REFERENCES

- Bechini, R., L. Baldini, R. Cremonini, E. Gorgucci, 2008: Differential Reflectivity Calibration for Operational Radars. *J. Atmos. Oceanic Technol.*, **25**, 1542–1555.
- Bringi, V. N., and V. Chandrasekar, 2001: Polarimetric Doppler Weather Radar: Principles and Applications. Cambridge University Press, 636 pp.
- Evans, G.E., 1990: Antenna Measurement Techniques. Artech House, 229 pp.
- Goddard, J. W. F., J. Tan, and M. Thurai, 1994: Technique for calibration of meteorological radars using differential phase. *Electron. Lett.*, **30**, 166–167.
- Gorgucci, E., G. Scarchilli, and V. Chandrasekar, 1992: Calibration of radars using polarimetric techniques. *IEEE Trans. Geosci. Remote Sens.*, **30**, 853–858.
- Pratte, J. F., and D. G. Ferraro, 1989: Automated solar gain calibration. Preprints, 24th Conf. on Radar Meteorology, Tallahassee, FL, Amer. Meteor. Soc., 619–622.
- Rinehart, R. E., 1978: On the use of ground return targets for radar reflectivity factor calibration checks. *J. Appl. Meteor.*, **17**, 1342–1350.
- Scarchilli, G., E. Gorgucci, V. Chandrasekar, and A. Dobaie, 1996: Self-consistency of polarization diversity measurement of rainfall. *IEEE Trans. Geosci. Remote Sens.*, **34**, 22–26.
- Seliga, T. A., V. N. Bringi, and H. H. Al-Khatib, 1979: Differential reflectivity measurements in rain: First experiments. *IEEE Trans. Geosci. Electron.*, **17**, 240–244.
- Silbertstein, D. S., D. B. Wolff, D. A. Marks, D. Atlas, and J. L. Pippitt, 2008: Ground clutter as a monitor of radar stability at Kwajalein, RMI. *J. Atmos. Oceanic Technol.*, **25**, 2037–2045.
- Smith, P. L., Jr., 1974: The measurement of antenna gain in radar systems. *Microwave J*, **17**, 4 (April), 37-40.
- Tapping, K., 2001: Antenna calibration using the 10.7 cm solar flux. Preprints, Workshop on Radar Calibration, Albuquerque, NM, Amer. Meteor. Soc. [Available online at http://www.k5so.com/RadCal_Paper.pdf].
- Whiton, R. C., P. L. Smith, and A. C. Harbuck, 1976: Calibration of weather radar systems using the sun as a radio source. Preprints, 17th Conf. on Radar Meteorology, Seattle, WA, Amer. Meteor. Soc., 60–65.

Draft

Appendix: Tables

Documenting operations is a crucial aspect of calibration and of other maintenance operation as well. The following tables referenced in the text are a useful tool to track operations and record results of calibration.

Draft

Table 1: Summary of Transmitter Power Measurements

Date	Remarks	Instrument	H Channel		V Channel	
			<i>Peak</i> (dBm/kW)	<i>Average</i> (dBm/W)	<i>Peak</i> (dBm/kW)	<i>Average</i> (dBm/W)

Specify in Remarks: (A: average power sensor, P: peak power sensor)

Table 2: Antenna Gain Measurements (horn transmitting to radar antenna)

Quantity Date	P_t (dBm)		Received Power (dBm)				G_e (dB)	
			IF		RF P_r			
	<i>H Channel</i>	<i>V Channel</i>	<i>H Channel</i>	<i>V Channel</i>	<i>H Channel</i>	<i>V Channel</i>	<i>H Channel</i>	<i>V Channel</i>

Table 3: Antenna Gain Measurements (horn receiving method)

Date	P_t (dBm)		P_r (dBm)*		G_e (dB)	
	<i>H Channel</i>	<i>V Channel</i>	<i>H Channel</i>	<i>V Channel</i>	<i>H Channel</i>	<i>V Channel</i>

Table 4: Antenna Gain Measurements (solar calibration)

Date	S (SFU)	S (SFU) converted	T_a (K)		T_s (K)		G_e (dB)	
			<i>H</i> Channel	<i>V</i> Channel	<i>H</i> Channel	<i>V</i> Channel	<i>H</i> Channel	<i>V</i> Channel

Table 5 - Return-Loss Measurements

Date	Remarks	Return Loss (dB)	
		<i>H Channel</i>	<i>V Channel</i>

Table 6 - Summary of RSP Calibrations

Date	Remarks	Channel (H/V)	RF Noise (dBm)	IF Noise (dBm)	Conv. Gain (dB)	Reflectivity Baseline (dBz)

Channel is H or V

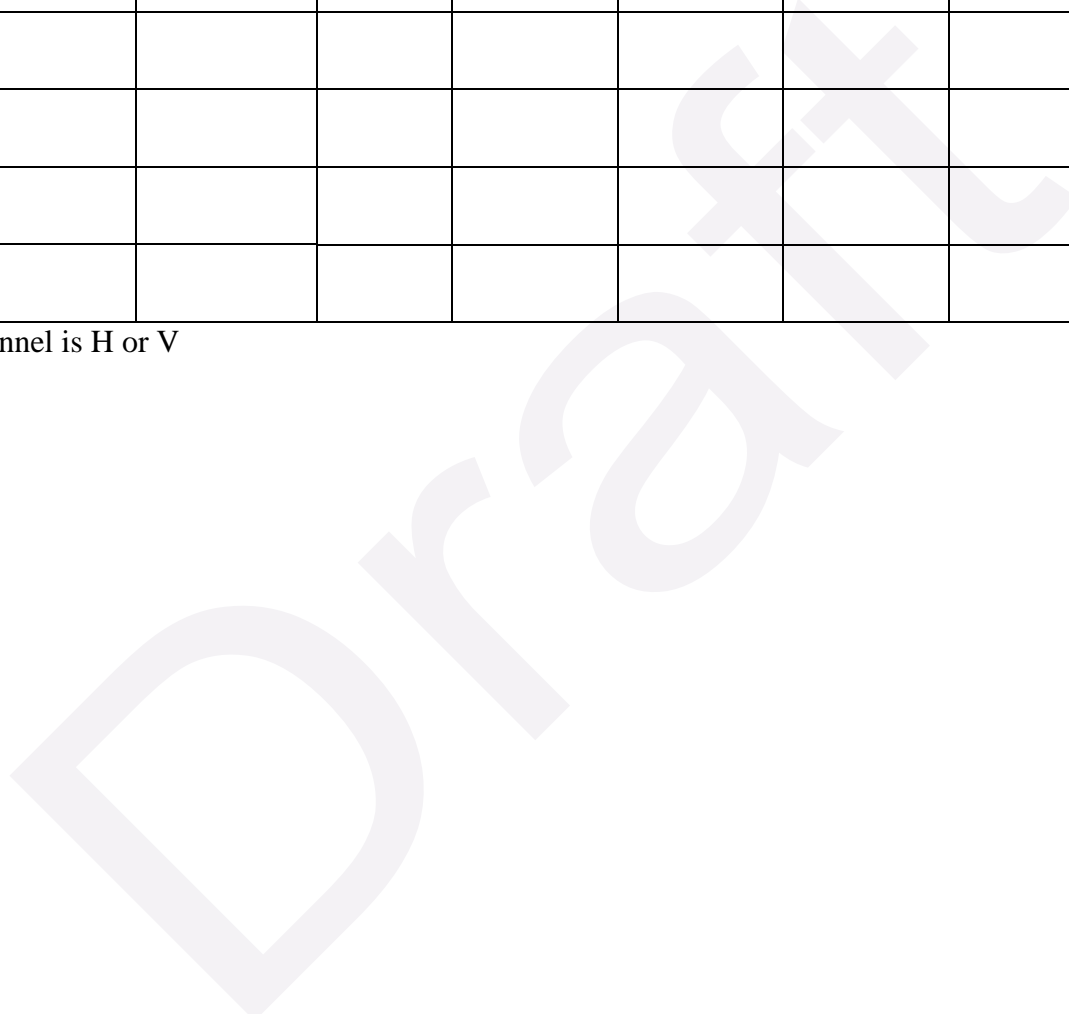


Table 7 - Some Characteristics of the FIR Filter

Date	Quantity	Pulse 1	Pulse 2	Pulse 3

Typical quantities are:

Filter loss (dB)

Noise bandwidth (MHz)

3 dB bandwidth (MHz)

6 dB bandwidth (MHz)

Table 8 - Receiver Noise Levels

Date	Remarks	IF Noise Power Level (dBm)		Difference (H-V) (dB)	Equiv. Difference at RF (dB)
		<i>H Channel</i>	<i>V Channel</i>		

Table 9 - Noise Figure/Bandwidth Measurements

Date	Signal Source	H IF Power (dBm)	V IF Power (dBm)

Signal Source can be a Dummy Load or a Noise Source.

Table 10 - Radar average power received at horn (up-link)

Date	Remarks	H Channel (dBm)	V Channel (dBm)	Difference (dB)

Table 11 - Test signals received (at IF) in H and V channels (downlink)

Date	Remarks	H Channel (dBm)	V Channel (dBm)	Difference (dB)

Table 12 – Waveguide measurements

Date	Path	Loss (dB)	Frequency behavior

Path is referred to reference block scheme of the radar in use

Table 13 - Directional couplers

Date	Quantity	Type	Forward (dB)	Reverse (dB)

Types:

Cross-guide
Bidirectional

Quantity:

Total Xmit power
H channel
V channel
H (antenna)
V (antenna)